Two distinct mechanisms underlie dosage sensitivity in Pumilio1-associated diseases

Salvatore Botta[1,2], Nicola de Prisco[1], Alexei Chemiakine[1], Maximilian Cabaj[1], Vicky L. Brandt[1], Purvi Patel[3], Rajesh K. Soni[3], and Vincenzo A. Gennarino[1,4,5,6,7]

[1]Department of Genetics and Development, Columbia University Irving Medical Center, New York, NY.
[2]Department of Translational Medical Science, University of Campania Luigi Vanvitelli, Caserta, Italy.
[3]Proteomics and Macromolecular Crystallography Shared Resource, Herbert Irving Comprehensive Cancer Center, Columbia University Irving Medical Center, New York, NY.
[4]Departments of Pediatrics and Neurology, Columbia University Irving Medical Center, New York, NY.
[5]Columbia Stem Cell Initiative, Columbia University Irving Medical Center, New York, NY.
[6]Initiative for Columbia Ataxia and Tremor, Columbia University Irving Medical Center, New York, NY.
[7]Lead contact and corresponding author: vag2138@cumc.columbia.edu

KEYWORDS
Pumilio1 interactome, RNA-binding proteins, PUM2, FMRP, AGO2, CCR4-NOT, RBFOX3, PADDAS, PRCA.

HIGHLIGHTS

- RNA-binding proteins can cause disease via their targets or interactors
- Interactions among RNA-binding proteins can differ by brain region and sex
- A modest reduction in PUM1 levels affects PUM1-specific targets
- Greater reductions in PUM1 levels disrupt interactors and shared targets

SUMMARY

The RNA-binding protein (RBP) Pumilio1 (PUM1) is associated with two distinct diseases: a late-onset ataxia and a neurodevelopmental syndrome. The ataxia patients retain 75% of normal PUM1 levels, the syndromic patients ~50%, but this seems inadequate to explain the difference in phenotypes. We hypothesized that mild disease results from dysregulation of PUM1 targets, whereas severe disease involves disruption of PUM1 complexes and deregulation of shared targets. We therefore developed a PUM1 interactome for the murine brain and found that PUM1 shares targets with several RBP interactors (PUM2, FMRP, AGO2, and RBFOX3). PUM1 haploinsufficiency destabilizes these RBPs to varying degrees by brain region and sex, and alters expression of their shared targets, but the milder disease-causing mutation affects only PUM1-specific targets. These data indicate that dosage-sensitive proteins can produce different phenotypes by different mechanisms, and that there may be more intimate cooperation among RBPs than expected.

INTRODUCTION

To respond with agility to a specific perturbation, cells must adjust their gene expression, much of which is controlled at the post-transcriptional level by RNA-binding proteins (RBPs). RBPs regulate RNA localization, transport, translation, splicing, and decay, and they orchestrate hundreds of pathways that are responsible for proper biological functions (Hentze et al., 2018; Keene, 2007). RBPs can coordinate or compete with each other (Dassi, 2017), and they also interact with microRNAs, which are small non-coding RNAs that suppress the expression of their target genes by binding to a short complementary seed region in the 3' UTRs of mRNAs. The RBP and microRNA machinery are particularly important in neurons, whose plasticity demands a rapid response to stimuli despite their extreme morphology (Mauger et al., 2016). Indeed, RBPs are associated with several syndromes that affect motor control, behavior, and cognition: for example, mutations in FMRP underlie the developmental disorder Fragile X syndrome, but milder "premutations" in FMRP cause adult-onset Fragile X-associated tremor and ataxia syndrome (FXTAS) (Lukong et al., 2008). The RBPs TDP43 and FUS are involved in amyotrophic lateral sclerosis, with TDP43 mutations also linked to frontotemporal dementia (Ravanidis et al., 2018). Despite recent interest in these and other RBPs implicated in neuronal function, we still know relatively little about their workings, their interactions, or their regulation (Darnell and Richter, 2012; Khalil et al., 2018; Ravanidis et al., 2018).

We recently found that the RBP Pumilio1 (PUM1) is involved in two distinct human diseases (Gennarino et al., 2018; Gennarino et al., 2015). PUM1-associated developmental delay and seizures (PADDAS) is an early-onset neurodevelopmental disorder, while PUM1-related cerebellar ataxia (PRCA) is a slowly progressive, mild ataxia with onset in mid-life. Although the severity of the PRCA and PADDAS phenotypes tracks with the levels of functional PUM1 (75% of wild-type levels in PRCA, 40-60% in PADDAS), precisely what is happening at the molecular level was unclear. PUM1 comprises a highly conserved RNA-binding domain composed of eight tandem repeats known as Puf homology domains (HDs), and the mutation that produces mild disease (PRCA), T1035S, lies within this domain and impairs RNA binding—but the most severe PADDAS mutation (R1147W) is outside this domain and does not seem to impair RNA binding (Gennarino et al., 2018; Gennarino et al., 2015). Moreover, the PADDAS phenotype is wide-ranging and variable. The most severe mutation, R1147W, causes small stature, physical dysmorphologies, cognitive and language delays, motor impairments, and seizures starting in infancy. On the other hand, our female R1139W patient did not have cognitive deficits, seizures, or dysmorphologies, and the onset of her motor features was around 4 years of age (Gennarino et al., 2018; Gennarino et al., 2015); the onset of motor features in a newly identified male patient was delayed until 10 years of age (personal communication). The enormous difference in phenotypic outcomes between mutations in the RNA-binding domain and outside of it, plus the fact that the six then-known PUM1 targets were upregulated to similar extents in the PRCA and PADDAS patient cell lines (Gennarino et al., 2018), led us to hypothesize that PRCA is caused by deregulation of PUM1 targets, but that PADDAS results from disruption of PUM1's interactions with its protein partners along with de-repression of the targets of these complexes.

To test this hypothesis would require knowing both PUM1 targets and interactors in the mouse brain. Little is known about PUM1 function in the brain, however. Most of what we do know comes from studies of development (Goldstrohm et al., 2018). As a member of the PUMILIO/FBF (PUF) family of RBPs that contains its close homologue Pumilio2 (PUM2), PUM1 was initially discovered in *Drosophila* for its contributions to embryonic patterning (Lin and Spradling, 1997) and stem cell maintenance (Leeb

et al., 2014). Studies in fly, worm, and germ cells show that Pumilio proteins regulate mRNA targets through at least three distinct mechanisms: they can collaborate with the microRNA machinery to repress targets (Friend et al., 2012; Kedde et al., 2010; Miles et al., 2012); they can recruit the CCR4-NOT deadenylase complex to shorten poly(A) tails and promote mRNA degradation (Temme et al., 2014; Van Etten et al., 2012; Weidmann et al., 2014); and they can antagonize poly(A)-binding proteins to repress translation (Goldstrohm et al., 2018). There is also evidence that PUM1/2 can activate certain mRNAs (Goldstrohm et al., 2018).

Given that virtually nothing is known about PUM1 activities in the brain, we decided to take an unbiased approach by using *in vivo* proteomics to identify PUM1's native partners. We examined the brain as a whole as well as three brain regions that most highly express PUM1. We then determined the effect of PUM1 loss on a focused subset of RBP interactors, using *Pum1* heterozygous and knockout mice and patient-derived cell lines. We also identified targets shared among these interactors and examined their responses to PUM1 insufficiency in mice and cell lines from patients bearing the T1035S and R1147W mutations. (Note that, because we deal with both mouse and human proteins in this paper, we will refer to the mouse proteins with lower case (e.g., Pum1) and the human proteins in all caps (PUM1).)

RESULTS

Establishing the Pumilio1 interactome across the adult mouse brain

To identify Pum1 protein partners, we performed co-immunoprecipitation (IP) for Pum1 on whole brains from 10-week-old wild-type mice, followed by liquid chromatography with tandem mass spectrometry (LC-MS/MS, or simply mass spec); we used IP against IgG (IP-IgG) as a negative control (see Methods). Because of the intrinsic variability of the mass spec technique, we combined and homogenized whole brains from two 10-week-old wild-type mice per sample (1 female and 1 male), aliquoting half of each sample for IP against either Pum1 or IgG, then performed six biological replicates (six samples, 12 mice total) for each mass spec experiment against IP-Pum1 and IP-IgG. Post-IP western blot detected no residual Pum1 from brain tissue, confirming that our protocol recovers virtually all of Pum1 (**Figure S1A**).

Principal component analysis (PCA) readily separated the IP-Pum1 interactors from the control IP-IgG (**Figure S1B**). To increase the likelihood that our candidates would prove to be genuine interactors, the proteins had to have at least two unique peptides present in at least five out of six IP-Pum1 samples and also show at least an average >1.5-fold difference between IP-Pum1 and IP-IgG in label-free quantification intensity (LFQ-intensity, see Methods). Our analysis yielded 412 putative Pum1 interactors (**Figure 1A** and **Table S1**). To begin to understand how some of these proteins relate to each other, we incorporated mammalian protein-protein interaction data from CORUM and the Human Protein Atlas by using g:GOSt (g:Profiler; see Methods) (Raudvere et al., 2019) to reveal 22 clusters of functionally related proteins (**Figure 1A**). Among the putative interactors were those that have been previously identified, supporting the validity of our approach. For example, our mass spec identified Nanos1, the mammalian homologue of *Drosophila* Nanos, which was one of the first proteins found to interact with Pumilio during fly development (Wang et al., 2001); it also identified Pum2 and Fmrp, which associate with Pum1 in neural progenitor cells (Zhang et al., 2017). Some of the identified proteins belong to families previously found to interact with PUM1 *in vitro*, such as Cnot1, which is the central scaffold of the CCR4-NOT complex (Enwerem et al., 2021; Van Etten et al., 2012). Translation initiation factors (cluster 3) have been found to cooperate with Puf proteins (Blewett and Goldstrohm, 2012), and human

PUM2-mediated repression was found to require PABPC1, while our mass spec yielded Pabpc4 (Weidmann et al., 2014). Interestingly, neither Nanos1 nor Pabpc4 belong to clusters. Cluster 8 had the most previously identified Pum1 interactors and was the most strongly interconnected with other clusters.

There were a number of proteins that have never been associated with PUM1. Many members of the anaphase-promoting complex (cluster 21) were among the candidate interactors with the greatest fold-change. This E3 ubiquitin ligase complex targets substrates for degradation and is essential for neuronal survival (Almeida et al., 2005; Gieffers et al., 1999; Sivakumar and Gorbsky, 2015). We performed preliminary validation by reciprocal co-IP between Pum1 and Anapc1, which scaffolds the APC/C complex, and between Pum1 and Fzr1, which forms its catalytic pocket (Sivakumar and Gorbsky, 2015) (**Figure S1C, D**). Cluster 11 was also unexpected, as it contains members of both mTORC1 (Rptor, Cad, Tsc1, Tsc2) and mTORC2 (Rictor) pathways, which are involved in a variety of cellular functions from promoting cell growth to autophagy (Liu and Sabatini, 2020). Reciprocal co-IP with Rptor and Cad confirmed interactions with Pum1 (**Figure S1C, D**).

Given the plethora of putative interactors to investigate, we repeated the mass spec experiments on the cerebellum, hippocampus, and cortex, where PUM1 is most highly expressed (Gennarino et al., 2015), to see which pathways emerged as predominant. Because our mass spec protocol requires at least 5 mg of protein, we combined cerebellar tissue from eight 10-week-old wild-type mice (4 female and 4 male), performing the experiment in triplicate (for a total of 24 mice); we did the same for cortical tissue. For the hippocampus, we combined tissues from ten wild-type mice (5 of each sex) for three experiments (30 mice; see Methods). As before, we selected proteins with at least two unique peptides and an average of >1.5 fold-change between IP-Pum1 and the IP-IgG. PCA again showed a clear separation of Pum1 samples from the IgG and indicated that the Pum1 hippocampal and cortical interactomes are more similar to each other than to that of the cerebellum (**Figure S2A**). We identified 854 putative Pum1 interactors in the cerebellum, 423 in the hippocampus, and 598 in the cortex (**Table S1**). 467 putative interactors were unique to the cerebellum, 140 to the hippocampus, 229 to the cortex, and 154 unique to the rest of the brain (i.e., excluding these three regions). Only 88 candidates were shared among these three brain regions and the whole brain (**Figure S2B**, yellow dots; **Figure S2C**). To our surprise, the only brain region to show interaction between Pum1 and Pum2 was the cortex (**Figure S2C**).

The region-specific proteins expanded the list of Pum1 interactors in the pathways described initially (**Figure S2D-F**). For example, we found not only Cnot1 in all three brain regions, but also Cnot2 and Cnot10 (which appears to be cortex-specific) (**Figure S2F**). There were many proteins involved in translation initiation, with Eif3b being specific to the hippocampus (**Figure S2B**). Rbfox1 was specific to the cortex, and Rbfox2 to the cerebellum (**Figure S2B**), consistent with previous work showing that Rbfox1 mediates cell-type-specific splicing in cortical interneurons (Wamsley et al., 2018) and that Rbfox2 is needed for cerebellar development (Gehman et al., 2012). The brain-region-specific analysis did not yield many additional interactors in the APC/C (**Figure S2D**) or mTOR pathways (**Figure S2E**). It did, however, reveal many pathways that have never been associated with Pum1 (**Table S1**). Taken as a whole, these data suggest that the RNA-silencing, CCR4-NOT, translational initiation, polyA regulation, and splicing machineries are fine-tuned according to brain region or neuronal cell types, whereas the APC/C and mTOR machineries remain fairly consistent, at least across these three brain regions.

This is not to say that certain interactions are necessarily limited to these brain regions. They may occur in regions not tested; they may occur across the whole brain, but at levels that did not reach the threshold we set. It could also be that some interactors are expressed more highly in specific brain

regions, though this is not the determining factor for the interaction with Pum2, which is expressed to an equivalent degree in all three brain regions (**Figure S2G**).

We then performed DAVID Gene Ontology analysis for the hits from both the whole brain and each brain region (**Figure 1B** and **Tables S2**). The dominant categories were ubiquitin ligases (anaphase-promoting complex [APC/C], E2/E3 and Kll-linked ubiquitin) and RBPs involved in various aspects of RNA metabolism (RNA silencing, 3'UTR binding, mRNA stability, transport, and splicing). We decided to prioritize the RBPs in cluster 8 (**Figure 1A**)—Fmrp and Ago2 (involved in RNA silencing), Pum2, Cnot1, and Rbfox3 (an alternative splicing factor)—for three reasons. First, this cluster was the most highly interconnected with other clusters; second, RNA-related categories were prominent in the gene ontology analyses for both whole brain and all three brain regions; and third, these RBPs have been well studied and would allow us to more readily test the consequences of PUM1 loss.

Pum1 associates with Pum2, Fmrp, Ago2, and Cnot1 in the absence of mRNA

We first performed co-IP followed by western blot to confirm Pum1 association with Pum2, Fmrp, Ago2, Rbfox3 and Cnot1 (**Figure 2A**, *left panel*). Because Fmrp and Ago2 both bind Mov10 *in vitro* (Kenny et al., 2020; Kenny et al., 2014), we also blotted for murine Mov10, even though it did not appear among our mass spec results. Mov10 did interact with Pum1, likely in concert with Fmrp (**Figure 2A**). Reciprocal co-IP using antibodies against Pum2, Ago2, Fmrp, Rbfox3, Cnot1, and Mov10 followed by western blot confirmed these interactions (**Figure 2B**). To verify the specificity of the antibodies, we IPed all six RBPs in *Pum1*$^{-/-}$ mouse brain and detected none of them (**Figure S3A**). As negative controls, we tested other proteins associated with the RISC complex (Ago1 and Ago3) that did not appear in our mass spec data, and our IP experiments found no interactions (data not shown).

To determine whether these RBP interactions require the presence of RNA—and to exclude the possibility that the IPs simply recovered other proteins that are co-bound to target RNAs but are not part of the same complex as the protein of interest—we treated the mouse brain samples with RNase and verified that no detectable RNA remained (see Methods). Pum1 still associated with Pum2, Fmrp, Ago2, and Cnot1 in the absence of mRNA, but not Rbfox3 or Mov10 (**Figure 2A**, *right panel*). Interestingly, a previous *in vitro* study found that PUM1 associates with AGO2 only in the presence of RNA in T-REx 293 cells (Sternburg et al., 2018). We repeated these RNase experiments in HEK293T cells, which confirmed these results (except for RBFOX3, which was not detectable in these cells) (**Figure 2C**).

Some interactions among these RBPs require PUM1

We next performed reciprocal co-IP in wild-type (WT) and *Pum1*$^{-/-}$ 10-week-old mouse brains for Pum2, Ago2, Fmrp, Cnot1, Rbfox3, and Mov10. Pum2 interacted with Cnot1 only in the presence of Pum1 (**Figure 3A**). Unexpectedly, Fmrp interacted with Mov10 and Rbfox3 only in the presence of Pum1 (**Figure 3B-D**). Fmrp and Cnot1 did not associate in the wild-type mouse brain (**Figure 3B**, *left*) but they did so in the absence of Pum1 (**Figure 3B**, *right*). Ago2 associated with Pum1, Fmrp, Cnot1 and Mov10 in WT mouse brain, but in the absence of Pum1 it no longer interacted with Fmrp or Mov10 (**Figure 3E**). Rbfox3 associated with Cnot1 (**Figure 3C**) but not *vice versa* (**Figure 3F**). IPs against Pum2, Ago2, Fmrp, Cnot1, Rbfox3, and Mov10 with and without RNase treatment in WT and *Pum1*$^{-/-}$ mouse brains (**Figure S3B-G**) confirmed that, in the absence of Pum1, these interactions require RNA.

In summary, Pum1 associates with Pum2, Fmrp, Ago2, Cnot1, with or without RNA (**Figure 3A-F** and **Figure S3B-G**). Pum1 seems to be required for Fmrp to interact with Mov10 and Rbfox3, and for

Ago2 to interact with Fmrp, Mov10, and Cnot1. In the absence of Pum1, the interactions between Pum2, Fmrp, Ago2 and Cnot1 require RNA (**Figure S3B-G**).

Pum1 loss alters RBP levels by brain region and sex

If these are *bona fide* interactors of Pum1, then we would expect loss of Pum1 to affect their expression levels. *Pum1* heterozygous and knockout mice showed changes in the levels of Pum2, Ago2, and Mov10 proteins across the brain (**Figure S4A**), but only *Pum2* showed changes in mRNA levels (**Figure S4B**). Interestingly, Ago2 and Mov10 levels fell only in male mice (**Figure S4A**), so we decided to pursue this sex difference by brain region. We quantified Pum2, Fmrp, Ago2, Rbfox3, Cnot1 and Mov10 in the cerebellum, cortex, and hippocampus. We first measured Pum1 mRNA and protein levels to confirm the reduction of Pum1 in our *Pum1*$^{+/-}$ or *Pum1*$^{-/-}$ mice in each brain region (**Figure 4A-C,** and **S5A**). Pum2 protein levels increased in all three brain regions, as did its mRNA (**Figure 4A-C,** and **S5A**).

Fmrp protein levels were upregulated in all three brain regions in male KO mice, but in female KO cerebella Fmrp was reduced by almost 70% (**Figure 4A**). (We should note that sex differences in Fmrp expression have been previously reported (Singh et al., 2007; Singh and Prasad, 2008).) Three other proteins also showed divergent responses to Pum1 loss according to sex and brain region: Ago2 (up in female but down in male cerebella, with the opposite pattern in hippocampus and cortex), Rbfox3 (in the hippocampus), and Cnot1 (in the cerebellum) (**Figure 4A-C**). None of them showed any changes in mRNA levels (**Figure S5A**), despite the fact that *Fmr1* and *Cnot1*, like *Pum2*, have a Pumilio recognition element (PRE) (Zamore et al., 1997) in their 3'UTR. It may be that the loss of Pum1 causes sex- and region-specific reorganization of these complexes, or that there are additional sex-specific Pum1 interactors.

Pum1 loss dysregulates Ago2 and the microRNA machinery in mouse cerebella by sex

Since loss of Pum1 function has deleterious effects on the cerebellum in both mice (Gennarino et al., 2015) and humans (Gennarino et al., 2018), we were curious to know whether the divergence of Ago2 protein levels in males and females extended to cerebellar miRNAs. We performed miRNAseq. Hierarchical heatmap clustering of miRNA expression in *Pum1*$^{-/-}$ and WT male and female cerebella at 10 weeks of age revealed that the expression of 166 miRNAs (**Table S3**) diverged between the two sexes in parallel with Ago2 levels (**Figure 4D**).

To examine the functional consequences of this Ago2/miRNA dysregulation, we looked at the expression of downstream targets that are co-bound by those miRNAs in 10-week-old wild-type and *Pum1*$^{-/-}$ male and female cerebella. We first selected all the miRNAs with at least a 25% change in expression in either direction, for a total of 19 miRNAs. Using TargetScan and CoMeTa (Agarwal et al., 2015; Gennarino et al., 2012) we identified 6832 putative targets that are co-bound by at least 2 out of 19 possible miRNAs. To reduce this list to a more manageable size for testing expression changes by qPCR, we prioritized targets that are co-bound by at least 8 miRNAs, for a total of 49 putative targets. *Pum1*$^{-/-}$ male and female cerebella showed gene expression changes for 44 out of these 49 targets, which correlated with the sex-dependent differences in Ago2 levels (**Figure 4E**, **S5B** and **Table S4**).

These data confirm that Pum1's interaction with Ago2 and the miRNA machinery is physiologically relevant. Moreover, loss of Pum1 affects miRNA expression and the levels of their targets in a sex- and brain region-specific manner. While sex-specific miRNA expression has been suggested for some miRNAs (Fuentes et al., 2018; Warnefors et al., 2017), to our knowledge there has been no report of

global sex-biased miRNA expression by dysregulation of Ago2.

The top targets of Pum1, Pum2, Fmrp, Ago2, and Rbfox3 are shared

So far our *in vivo* proteomics seems to be borne out by changes in the levels of protein interactors upon loss of Pum1. Ideally, we would purify recombinant proteins to perform gel filtration assays to get a better handle on the nature of the interactions, but we found Pum1 difficult to purify because it is prone to aggregation (data not shown). We therefore cannot say whether the interactions are direct, although the fact that our brain-region-specific mass spec identified new interactors in the same pathways that had not been pulled down from the whole brain (or other regions), despite their high expression, does support the notion that these interactions are real. We can predict, however, that if Pum1 forms complexes with these RBPs that are physiologically relevant, then they should share many of the same mRNA targets.

To test this hypothesis, we downloaded and reanalyzed all the high-throughput sequencing UV-crosslinking and immunoprecipitation (HITS-CLIP) data that is available from the murine brain. Fortunately, this data exist for Fmrp (Maurin et al., 2018), Ago2 (Chi et al., 2009), Rbfox3 (Weyn-Vanhentenryck et al., 2014), Pum1, and Pum2 (Zhang et al., 2017). Then, to determine whether and how much the targets overlap, we performed gene set enrichment analysis (GSEA) (Subramanian et al., 2005). GSEA is a method for determining whether members of a particular class of genes from set *S,* such as the targets of a particular RBP like Pum1, are randomly distributed throughout another gene set list *L*, which is ranked (in this case) according to reads per kilobase of transcript, per million mapped reads (RPKM). Genes from *S* that are enriched (over-represented) at the top of *L* are expressed more than would be expected; the converse is true for genes over-represented at the bottom of *L*. Here, we performed pairwise GSEA analysis using Fmrp as the basis for comparison (because it has the largest dataset) and Pum1, Pum2, Ago2 and Rbfox3. As negative controls, we used HITS-CLIP data from mouse brain for four RBPs that did not show up as Pum1 interactors in our mass spec: Mbnl2 (Charizanis et al., 2012), Nova (Zhang et al., 2010), Apc (Preitner et al., 2014), and Ptpb2 (Licatalosi et al., 2012).

Strikingly, Pum1 HITS-CLIP targets were preferentially distributed in the top 5th percentile of all Fmrp targets, with an enrichment score (ES) of 0.93 (the maximum is 1) and a FDR of 0 (**Figure 5A,** *blue line represents ES*). Pum2, Ago2, and Rbfox3 showed nearly identical patterns (**Figure 5A**). There was no significant overlap between the targets of Fmrp and those of any negative control (Nova had the highest ES, but this was only 0.36 with a rank max of 45th percentile and FDR=1; **Figure 5B**).

To ascertain whether the highest-ranking Fmrp targets correspond to the genes with the highest probability of being Pum1 targets, we performed a more detailed GSEA. We first divided the Fmrp ranked target list into 10 equal bins according to percentile. We then repeated GSEA of Pum1 HITS-CLIP data for each bin and found that 648 of the 1194 identified Pum1 targets (54%) are in the top 10th percentile of Fmrp targets, with an ES of 0.8; moreover, this was the only statistically significant bin (**Figure 5C**). This was also true for Pum2, Ago2, and Rbfox3 (**Figure 5C**). Neither Pum1, Pum2, Rbfox3, Fmrp, nor Ago2 targets were enriched among any of the target lists of the negative controls ranked by RPKM (**Figure S6A,** and data not shown).

We then performed the corresponding analysis using the Pum1 target list as the basis for comparison instead of the Fmrp list. We ran GSEA on each of the four Pum1 partners against the list of Pum1 target genes (again ranked by RPKM), and each partner's targets are within the top 20% of the Pum1 list (**Figure 5D**). Specifically, Fmrp's targets reside in the top 10th percentile (with an ES of 0.81), Pum2's targets within the 16th percentile (ES=0.9), Ago2's targets within the 18th percentile (ES=0.76), and

Rbofx3's targets within the 19th percentile (ES=0.67). The four RBPs used here as negative controls have a minimum rank at the 37th percentile, and the best ES was 0.26 for Apc; none of the five reached statistical significance (**Figure 5D**). These analyses demonstrate that there is substantial overlap among the highest-ranked targets of Pum1, Pum2, Fmrp, Ago2, and Rbfox3.

We then decided to look at the targets shared by Pum1, Pum2, Ago2, and Rbfox3 and see how they distribute within Fmrp. The result was striking, with an ES of 0.93 falling within the top 5th percentile (**Figure 5E**); 141 out of 175 common targets were within the top 10th percentile (bin 1) of Fmrp targets, with 99 within the top 5th (**Figure 5F** and **Table S5**). This contrasts with the negative controls, for which the best ES was 0.41 within the top 40th-60th percentile (**Figure 5G**). DAVID gene ontology analysis of those 175 common targets between Ago2, Pum1, Pum2, Fmrp, and Rbfox3 revealed pathways enriched in neurons and axonal projections (**Figure S6B** and **C**). Previous studies have shown that Pum1 and Pum2 cooperate with the microRNA machinery to suppress certain targets (Gennarino et al., 2015; Kedde et al., 2010). Among Fmrp HITS-CLIP targets, there were almost 300 microRNAs. Pum1 HITS-CLIP has 60 miRNAs, only four of which are not shared with Fmrp; Pum2 HITS-CLIP has no miRNAs that are not shared with either Pum1 or Fmrp (**Figure S6D** and **Table S6**).

Because neuronal genes tend to be long (Zylka et al., 2015) and RPKM can introduce bias toward longer genes (Mandelboum et al., 2019), we wanted to ensure that the targets were actually more highly expressed. Since the published HITS-CLIPs data from other studies were acquired from mice at different ages (but most at 3 weeks of age) and these studies did not typically perform RNAseq in parallel with HITS-CLIP from the same tissue and age, we decided to perform RNAseq from WT mice at 3 weeks of age in triplicate to determine a baseline level of gene expression in mouse brain expressed as DESeq2-normalized counts (Love et al., 2014) (see Methods and **Table S7**). We then normalized RPKM values and repeated the GSEA enrichment analysis. The enrichment between the targets of Pum1 and those of Pum2, Ago2, Fmrp, and Rbfox3 was retained even after gene expression normalization (**Figure S6E-G**), with a minimum ES of 0.78 compared to the negative controls (**Figure S6E, F**). The shared targets of Pum1, Pum2, Rbfox3, and Ago2 were even more enriched, with an ES of 0.84 (**Figure S6H**).

PUM1 interactors are destabilized in cell lines from PADDAS, but not PRCA, patients

Having identified PUM1 interactors and shared targets, we were now in a position to test our two-pronged hypothesis about how *PUM1* mutations can lead to different diseases. To determine whether either mutation destabilizes PUM1 interactors, we compared their levels in patient-derived cell lines with those in controls. For PADDAS, we compared fibroblasts from one 9-year-old female patient (R1147W; subject 1, or S1) with fibroblasts from three different 9-year-old female healthy controls. For PRCA, we compared lymphoblastoid cells from two female PRCA patients (both with the T1035S mutation; subjects 2 and 3, or S2 and S3, 59 and 58 years old, respectively) with lymphoblastoid cells from three different 58-year-old female healthy controls (Gennarino et al., 2018). We first measured how much PUM1 we could pull down from the patient-derived cell lines compared to their controls. Post-IP did not detect any residual PUM1 from PADDAS or PRCA cell lines, or their age-matched controls, confirming that our protocol was able to pull down virtually all of the PUM1 protein from patient-derived cell lines (**Figure S7A, B**). IP against PUM1 followed by western blot showed that PADDAS cells had 49%, and PRCA cells 76%, of the amount of PUM1 found in healthy controls (**Figure 6A** and **B**), consistent with our previous report (Gennarino et al., 2018).

Co-IP confirmed that PUM1 binds PUM2, FMRP, AGO2, CNOT1, and MOV10 in patient cell lines

(**Figure 6A** and **B**). The mild T1035S variant reduced PUM1 binding to AGO2 by ~21% (**Figure 6B**). The more severe R1147W variant, however, reduced PUM1 binding to AGO2, CNOT1, and MOV10 by ~84%, ~59%, and ~90%, respectively (**Figure 6A**). Binding with FMRP did not appear to be affected. (We could not examine the effect of PUM1 mutations on RBFOX3, which is not expressed in fibroblasts or lymphoblastoid cell lines.)

Western blot analysis revealed that the proteins that lose their interaction with the R1147W variant undergo reduction in their expression levels (**Figure 6C**). Note that MOV10, which was not identified by our mass spec, was greatly reduced in its interaction with R1147W (**Figure 6A**) but its protein levels remained unchanged (**Figure 6C**). AGO2 and CNOT1 levels were unchanged in the PRCA cell line but were ~50% lower in the PADDAS cell line (**Figure 6C**). The mRNA levels of *PUM1*, *AGO2*, *CNOT1*, and *MOV10* did not change (**Figure S7C**), confirming that the reductions in their respective protein levels were due to the loss of interaction with PUM1-R1147W.

One limitation of these studies is that we are implicitly comparing different cell types. Since we haven't been able to procure lymphoblasts from PADDAS patients or fibroblasts from PRCA patients, we sought to we sought to confirm our findings *in vitro*. We inserted a GST-tag at the N-terminal of *AGO2*, *CNOT1*, and *FMRP* (see Methods). (AGO2 and CNOT1 were the only proteins whose levels changed in fibroblasts, so FMRP is used here as a control.) We also cloned a Myc-tag polypeptide at the N-terminal of *PUM1*-WT, *PUM1*-R1147W (PADDAS) and *PUM1*-T1035S (PRCA) (see Methods). We then co-transfected the same amount of Myc-tagged PUM1 proteins with the GST-tagged interactors, followed by western blot to quantify the amount of GST-tagged protein retrieved relative to the quantity of PUM1 proteins pulled down in the IP. GST-AGO2 interacted with Myc-PUM1-R1147W 76% less than it did with Myc-PUM1-WT (**Figure 7A**), in alignment with our observations in the PADDAS cell lines (**Figure 6A, B**). We also found ~35% less interaction with CNOT1 (**Figure 7B**) but no decrease in PUM1 binding by FMRP (**Figure 7C**), again in accord with our findings in patient-derived cells (**Figure 6A**, **B**).

These data confirm that the R1147W mutation, which does not impair PUM1 binding to mRNA (Gennarino et al., 2018), does impair interactions with PUM1's native partners.

R1147W mutation dramatically destabilizes PUM1

We next tested the PUM1 variants in a protein stability assay. We measured the half-life of the three Myc-tagged PUM1 proteins by separately transfecting 125ng of each. After cycloheximide treatment (T0) to block translation, we quantified the amount of protein at different time points: 30min, 1h, 2h, 4h, and 5h, compared to T0 (**Figure S7D**). The half-life of PUM1-WT was roughly 5.5 hours, the half-life of PUM1-T1035S was ~2 hours, and that of PUM1-R1147W slightly less than 1 hour (**Figure S7D**).

We also wondered whether the R1147W mutation might be impaired in binding with WT PUM1. It has been thought that Puf proteins do not dimerize (Edwards et al., 2001; Zamore et al., 1999), but recent work supports this possibility (Qiu et al., 2019). We therefore co-transfected each of the Myc-tagged PUM1 variants with the same amount of GST-tagged *PUM1*-WT and used an empty vector as a negative control. First, we confirmed that IP against Myc-PUM1-WT pulled down GST-PUM1-WT. IP against Myc-PUM1-R1147W pulled down 51% of the total GST-PUM1-WT, while the interaction between Myc-PUM1-T1035S and GST-PUM1-WT remained unchanged (**Figure 7D**). The same interaction was observed after RNase treatment, suggesting that PUM1 dimerizes without RNA (**Figure S7E**). These data suggest that the R1147W mutation might exert a dominant-negative effect on wild-type PUM1.

The combination of lower protein levels and marked protein instability helps explain why the

R1147W phenotype is better represented by the *Pum1* null mice than by the heterozygotes (Gennarino et al., 2018).

Shared targets are upregulated in PADDAS but not PRCA

We had hypothesized that PRCA would involve dysregulation of PUM1 targets, whereas PADDAS would involve both destabilization of PUM1 interactors and dysregulation of downstream targets of those interactors. We therefore tested the effects of the T1035S and R1147W mutations on validated PUM1-specific targets (Chen et al., 2012; Gennarino et al., 2015; Zhang et al., 2017) that are not in the HITS-CLIP data for the other RBPs but are expressed in both fibroblasts and lymphoblasts. PUM1-specific mRNA were dysregulated to very similar extents in PRCA and PADDAS patient cells, with only a few targets being up to 20% more upregulated in PADDAS (**Figure 7E**).

We then examined the mRNA levels of all 175 targets shared between PUM1, PUM2, AGO2, FMRP, and RBFOX3 (**Figure 5E** and **Table S5**) in the same PRCA and PADDAS patient cell lines. Of these shared targets, 55 were expressed in both PADDAS fibroblasts and PRCA lymphoblastoid cells. Of these 55, 52 shared targets were upregulated in PADDAS but not in PRCA (**Figure 7F**), by an average of two-fold (ranging from a low of 121% for IDS to 347% for TLK1). There was little or no change in most of these targets in PRCA cells, though levels of CALM1, ATP2A2, CREB1, and GNAQ fell by ~40%, and CALM2, TAOK1, and UBE2A by ~20% (**Figure 7F**).

These results support our hypothesis that the symptoms observed in PRCA are attributable to the dysregulation of PUM1-specific target genes, while PADDAS involves both protein partner destabilization and dysregulation of the partner proteins' targets.

DISCUSSION

Since our initial study describing PUM1-related diseases (Gennarino et al., 2018), we and others have identified additional PADDAS and PRCA patients (Bonnemason-Carrere et al., 2019; Gennarino et al., 2018; Imaizumi et al., 2019; Lai et al., 2019). In our sample, R1147W accounts for the majority of PADDAS patients, and T1035S for the majority of PRCA, which supports the value of studying these particular two mutations as causing the most severe and the most mild forms of PUM1-related disease. The question that drove the present study is: why should the difference between 50% and 75% of normal PUM1 levels produce such different phenotypes, especially when R1147W is not impaired in binding to mRNA? Our data strongly support our hypothesis that the difference is not due to a linear increase in the de-repression of mRNA targets but is rather a function of an additional mechanism coming into play: the destabilization of numerous interactions and the de-repression of their downstream targets. We found changes in the levels of Pum2, Fmrp, Ago2, Mov10, Cnot1, and Rbfox3 in response to loss of Pum1 that depended on brain region and sex; we found changes in the levels of these proteins in patient cell lines, despite unchanged mRNA levels; our *in vitro* studies using Myc- and GST-tagged proteins showed that AGO2 and CNOT1 lose their interaction with PUM1-R1147W, which itself binds less to WT PUM1.

Diseases involving dosage-sensitive proteins

There are other dosage-sensitive proteins that produce different phenotypes depending on their expression level (Tan and Zoghbi, 2019), and our results raise the possibility that interacting complexes may be disrupted once expression falls below a certain threshold. What that threshold might be, exactly, is not clear, but for PUM1 it seems to be somewhere between the 75% of wild-type levels of PUM1 seen

in PRCA and the 60% level estimated for the R1139W mutation that produced a milder form of PADDAS (Gennarino et al., 2018). In this context it is worth noting that a recent study found that, below a threshold of ~70% of normal levels of FMRP, there were steep decreases in IQ for each further decrement in FMRP levels, even as small as 5-10% (Kim et al., 2019). The amount of loss that can be sustained for a given protein would likely depend on its usual abundance, and it is possible that for some proteins, the difference in phenotype between higher and lower levels may indeed reflect a linear progression from mild to severe. For example, a mutation in *MECP2* that reduces the protein levels by only 16% causes a mild form of Rett syndrome: the child develop normally until the age of two years, then regressed, lost acquired language and manual skills, and develop hand stereotypies (Takeguchi et al., 2020). She eventually regained the ability to repeat words in an echolalic fashion and never developed seizures, but the phenotype was clearly Rett syndrome. The relationship between protein levels and disease features in MeCP2-related disorders may be more linear because this protein is so extraordinarily abundant (Sandweiss et al., 2020). Similarly, in proteopathies such as Alzheimer's or Parkinson's disease, genetic duplications of *APP* or *SNCA* cause earlier onset of what is recognizably the same disease (Chartier-Harlin et al., 2004; Rovelet-Lecrux et al., 2006).

In contrast, there are diseases in which the phenotypes do not simply range from mild to severe versions of the same symptoms, but seem to take on a different character. The polyglutamine diseases, such as Huntington's disease and the spinocerebellar ataxias, come to mind, perhaps because it was through studying spinocerebellar ataxia type 1 (SCA1), that PUM1's role in neurological function was discovered (Gennarino et al., 2015). In the polyglutaminopathies, the disease-causing protein bears an abnormally expanded CAG tract that tends to expand upon intergenerational transmission. Although the range of normal and pathogenic repeat tract lengths differs from one polyglutamine disease to another, larger expansions are more unstable, cause earlier onset, and affect far more tissues than smaller expansions (Orr and Zoghbi, 2007). For example, adult-onset SCA7 presents as ataxia, but infantile SCA7 affects the entire nervous system, the heart, and the kidneys, and leads to death by two years of age (Bah et al., 2020). Another example is Huntington's disease, where the juvenile form frequently lacks the classic chorea yet produces seizures, which are not a feature of the adult-onset disease; brain morphometry is also quite different in adult- and juvenile-onset cases (Tereshchenko et al., 2019). In this family of diseases, therefore, the mechanism is technically the same—repeat expansion—but different tissues have different thresholds for the CAG repeats. In the case of PUM1-related disease, it seems that an additional mechanism comes into play for the more severe phenotypes, beyond upregulation of mRNA targets. Interestingly, FMRP, which is susceptible to the expansion of a CGG repeat, is also associated with very different diseases, through two different mechanisms. Very large expansions silence the gene and produce Fragile X syndrome, whereas premutations are thought to cause the adult-onset Fragile-X-associated tremor/ataxia syndrome through RNA toxicity (Salcedo-Arellano et al., 2020).

Implications of the interactome

It has never been clear how the various modes of action attributed to Pum1 or other RBPs relate to one another, in large part because studies typically focus on one protein or pathway at a time. Our data suggest that the three mechanisms of repression that have been proposed for PUM1 may be coordinated in neurons, insofar as PUM1, PUM2, FMRP, AGO2, MOV10, CNOT1 and RBFOX3 (and related proteins in specific brain regions) either interact directly or are so close to each other within the ribonucleosome that the loss of Pum1 or RNA can change the composition of the complexes that are identified by co-IP,

in ways that are specific to brain region and sex. In this context it is worth noting that a very recent study found alternative splicing is altered in hippocampal slices from Fmrp-deficient mice; this observation was attributed to changes in H3K36me3 levels (Shah et al., 2020). Our data suggest that FMRP has an even closer relationship with the RBFOX protein family and alternative splicing machinery than suspected. Indeed, recent work has provided tantalizing glimpses of close interactions among various kinds of RNA metabolism. For example, members of the RBFOX family of proteins may, depending on their interactors (and perhaps cell type, sex, age, and species), be involved in microRNA processing in the nucleus and translation in the cytoplasm (Conboy, 2017). The FMRP/MOV10 complex appears to be involved in regulating translation through miRNA, with evidence that this role may change according to cell type (Kenny et al., 2020). Another study used quantitative mass spec to examine how Fmrp expression levels change with age in the wild-type rat dentate gyrus, and found differences in the levels of myriad proteins; among the 153 proteins with the most significant changes in levels were Pum1, Pum2 and Papbc1 (Smidak et al., 2017). The region-, sex-, and age-specificity of certain interactions indicates that unraveling RBP interactomes *in vivo* will require considerable finesse.

Although we did not pursue the entire interactome here, future studies investigating the interactions with members of the mTOR pathway and anaphase-promoting complex should be very fruitful. As we were preparing this work, a new study demonstrated that mTORC1 is involved in postsynaptic responses in hippocampal glutamatergic neurons, whereas mTORC2 modulates presynaptic release (McCabe et al., 2020). Given the importance of proteostasis at the synapse—and its failure in many neurological diseases (Zoghbi and Bear, 2012)—the close coordination of different protein-regulating activities is intuitively appealing.

There is still much to be understood about how PUM1 works, and where and how the various RNA metabolic machineries come into contact. The fact that several interactions we tested are RNA-independent suggests that certain complexes may form prior to binding mRNA. Could different pools of PUM1 form different complexes that adopt conformations that determine whether and where a target is bound? Do the subtle differences between brain regions in the choice of interacting partners from the same pathways influence target choice, activity, or both? Given that mRNA is much larger than proteins, is the quantity of these RBPs so great that they coat the RNA? What other proteins may be involved in 'handing off' an mRNA from one pathway to another? Although we began this study to better understand Pum1 functions in neurons, and thus have been rather Pum1-centric, it is by no means certain that Pum1 is the only protein that links these different molecular machineries. It may be simply the first of several missing links that we didn't realize were missing. Creating RBP interactomes should lead to a more complex yet realistic picture of RBP roles in neuronal function and in neurological disease.

ACKNOWLEDGMENTS

We thank the patients, their families, and their clinical teams for participating in our study, and the anonymous reviewers for helpful suggestions. We thank Mingyu Cao for help with statistical analyses and U.N. Wasko for starting the cloning procedure with Myc and GST tag sequences *in vitro*. We also thank G. Struhl, V. Ambros, T. Duchaine, G. Karsenty, H. Zoghbi, M. Jovanovic, Y. Giardina, and members of the Gennarino laboratory for helpful discussions and support. This work was supported by the National Institute of Neurological Disorders and Stroke (NINDS; R01NS109858 to V.A.G.); the National Ataxia Foundation/Young Investigator Research Grant (V.A.G.); the Brain & Behavior Research

Foundation Young Investigator Award; and the Paul A. Marks Scholar Program, Columbia University Vagelos College of Physicians and Surgeons. This project was also supported by the Genomic and RNA Profiling Core at Baylor College of Medicine and the Bioinformatics Core at the Jan and Dan Duncan Neurological Research Institute. The authors declare no competing interests.

AUTHOR CONTRIBUTIONS

S.B. designed and performed molecular experiments, analyzed and interpreted the data, and drafted the manuscript. N.D.P. performed the qPCR experiments, *in vitro* immunoprecipitation assays, analyzed the data, and edited the manuscript. A.C. performed all the brain region dissections in mice, performed the qPCR experiments and maintained the *Pum1* mutant mouse colony. M.C. performed the cloning experiments. V.L.B. interpreted data and drafted the manuscript. P.P and R.K.S. performed mass spectrometry and helped analyze the data. V.A.G. conceived the study, analyzed and interpreted the data, performed molecular experiments, and drafted the manuscript.

DECLARATION OF INTERESTS

The authors declare not competing interests

MAIN FIGURE TITLES AND LEGENDS

Figure 1. A brain-specific Pum1 interactome. (**A**) Network of putative Pum1 interactors in 10-week-old mouse brain (circles connected to Pum1 by gray lines). Interactions between interactors (purple lines) inferred by g:GOSt from Corum and the Human Protein Atlas (see Methods). The proteins in each of the 22 clusters are listed to the right. (**B**) Bubble plots show the top categories from gene ontology analyses of Pum1 interactors from whole brain, hippocampus, cortex, and cerebellum. Only the categories with fold enrichment >1.5 and FDR<0.05 are shown; not all are labeled because of space limitations (see **Table S2**).

Figure 2. Validation of Pum1 associations with key RNA-binding proteins (RBPs) in mouse brain. (**A**) Representative western blot of proteins pulled down by IP against Pum1 compared to IgG from wild-type mice brain without (*left*) and with (*right*) RNase treatment. In this panel, after IP-Pum1, we immunoblotted for Pum1 (positive control), Pum2, Fmrp, Ago2, Rbfox3, Cnot1, and Mov10. (See Methods.) (**B**) Representative western blot of the reciprocal IPs against Pum2, Fmrp, Ago2, Rbfox3, Cnot1 or Mov10. Each IP was immunoblotted against Pum1 and the putative interactor. (**C**) Representative western blots of the same proteins validated in panels **A** and **B** after IP against PUM1 with or without RNase treatment from HEK293T cell lines. In panels **A** through **C**, IP against IgG was used as a negative control and Input (1% from the initial protein lysate) as a loading control. The numbers on the right are the respective molecular weights expressed in kilodaltons (kDa). All the experiments were repeated at least six times. All mice were sacrificed at 10 weeks of age.

Figure 3. Pum1 interacts with several post-transcriptional RNA-binding proteins. Representative western blot of the proteins pulled down by (**A**) Pum2, (**B**) Fmrp, (**C**) Rbfox3, (**D**) Mov10, (**E**) Ago2, and (**F**) Cnot1 from WT and *Pum1*$^{-/-}$ mouse brain at 10 weeks of age. IP against IgG was used as negative control, and Input (1% from the initial protein lysate) as loading control. Molecular weights to the right are expressed in kilodaltons (kDa). All the experiments were repeated at least four times. Since Rbfox3

and Mov10 interactions with Pum1 are RNA-dependent we did not perform IP from *Pum1*$^{-/-}$ mouse brain.

Figure 4. Pum1 interactors and the microRNA machinery show brain region- and sex-specific responses to Pum1 loss. Representative western blots of Pum1, Pum2, Fmrp, Ago2, Rbfox3, Cnot1, and Mov10 in (**A**) cerebellum, (**B**) hippocampus, and (**C**) cortex in both male (left panel) and female (right panel) WT, *Pum1*$^{+/-}$, and *Pum1*$^{-/-}$ mice. The same number of males and females at 10 weeks of age was used for a total of at least 18 mice per genotype. Graphs below show quantification for each protein by brain region, sex, and genotype. All data were normalized to Gapdh protein levels. All experiments were performed at least 9 times per genotype from mice at 10 weeks of age (data represent mean ± SEM). *P* values were calculated by two-tailed Student's t test. *$p < 0.05$, **$p < 0.01$, ***$p < 0.001$. See **Figure S5A** for mRNA quantification for each interactor, brain region, and sex. P1 indicates Pumilio1. (**D**) Heatmap showing 166 microRNAs from mouse cerebellum in *Pum1*$^{-/-}$ male and female mice at 10 weeks of age that were dysregulated (fold change -3 to +3) relative to wild-type cerebellum. Three cerebella per genotype and sex were analyzed (see **Table S3** for the microRNA names and fold changes). (**E**) Heatmap showing mRNA quantification by qPCR for 49 targets co-bound by a minimum of eight dysregulated miRNAs (>20% change) from panel **D**. Three cerebella per genotype and sex were analyzed. Statistical significance and magnitude of dysregulation are illustrated for both male and female in **Figure S5B**.

Figure 5. Pum1 and its RNA-binding protein interactors share many neuronal mRNA targets. (**A**) Enrichment plots generated by Gene Set Enrichment Analysis (GSEA) of Pum1, Pum2, Rbfox3, and Ago2 HITS-CLIP targets plotted again Fmrp HITS-CLIP data ranked by RPKM. Pum1, Pum2, Rbfox3, and Ago2 targets are enriched at the top 10th percentile of the Fmrp targets with FDR=0. (**B**) GSEA analysis scores of HITS-CLIP data from each negative control (Apc, Nova, Ptpb2, and Mbnl2) plotted against Fmrp HITS-CLIP data ranked by RPKM. The negative controls have a maximum enrichment score of 0.36 for Apc ranking at the top 44.7% with FDR=1. (**C**) GSEA analysis scores of Pum1, Pum2, Rbfox3, and Ago2 HITS-CLIP data plotted against Fmrp HITS-CLIP data divided into 10-percentile bins and ranked by RPKM shows the shared targets are among the top percentiles of targets for each protein. (**D**) GSEA analysis scores of the HITS-CLIP data for Fmrp, Pum2, Ago2, Rbfox3 and four negative controls (Apc, Nova, Ptpb2, and Mbnl2) against PUM1 HITS-CLIP data ranked by RPKM. The targets of Fmrp, Ago2, Pum2, and Rbfox3 are enriched at the top 5th to 18th percentile of Pum1 targets. (**E**) GSEA analysis of the shared targets between Pum1, Pum2, Ago2, and Rbfox3 against Fmrp showing that they are enriched in the top 5th percentile of Fmrp targets ranked by RPKM. (**F**) Pum1, Pum2, Ago2, and Rbfox3 shared targets plotted against Fmrp HITS-CLIP targets ranked by RPKM and divided into 10-percentile bins shows that all of their respective targets are enriched at the top 10th percentile of the Fmrp targets ranked by RPKM. (**G**) GSEA analysis scores of the targets shared by Pum1, Pum2, Ago2, and Rbfox3 and the four negative controls (Apc, Nova, Ptpb2, and Mbnl2) plotted against Fmrp. At best the negative controls are enriched at the top 40% with a maximum ES of 0.41. For all the GSEA analyses, the False Discovery Rate (FDR) was provided by GSEA: **FDR<0.05 and ***FDR<0.01. ES=Enrichment score (blue line). Note that lowest rank at max percentage indicates stronger targets in the rank (see Methods).

Figure 6. The R1147W mutation, but not T1035S, destabilizes PUM1 interactors. (**A**) IP against PUM1 from PADDAS (R1147W) patient (Subject 1 or S1)-derived fibroblasts confirms the interactions

between PUM1 (used here as a positive control), and PUM2, FMRP, AGO2, CNOT1, and MOV10. *Bottom panel*: protein quantification shows loss of interaction between PUM1-R1147W and AGO2, CNOT1 and MOV10 compared to three age- and sex- matched control fibroblasts. Input (1%) was used as a loading control and IP against IgG was used as a negative control. (**B**) IP against PUM1 from two PRCA (T1035S) patient (S2 and S3)-derived lymphoblastoid cell lines confirm the interaction between PUM1 (used here as positive control), and PUM2, FMRP, AGO2, CNOT1, and MOV10. *Bottom panel*: Protein quantification shows a slight decrease in interactions with FMRP and AGO2, and a slight increase with CNOT1 and MOV10, compared to age- and sex- matched lymphoblastoid controls. Input (1%) was used as a loading control and IP against IgG was used as a negative control. In **A** and **B**, the amount of protein pulled down compared to IP-PUM1 was quantified as follows: $[IP^{X}/(Input^{X}/GAPDH^{X})]/[IP^{PUM1}/(Input^{PUM1}/GAPDH^{PUM1})]$, where X is the protein of interest. (**C**) Representative western blots (*left panels*) and relative quantification (*bar graphs to the right*) of protein levels for PUM1, PUM2, FMRP, AGO2, CNOT1, and MOV10 in PADDAS patient-derived fibroblasts and PRCA patient-derived lymphoblastoid cells compared to their respective age- and sex- matched fibroblast (for PADDAS patients) and lymphoblastoid (for PRCA patients) controls. Data were normalized to Gapdh protein levels. From **A** to **C**, all the experiments were performed at least six times. Data represent mean ± SEM. P values were calculated by two-tailed Student's t test. $*p < 0.05$, $**p < 0.01$, $***p < 0.001$.

Figure 7. RBP complexes with PUM1 R1147W are destabilized *in vitro* and shared neuronal targets are upregulated only in PADDAS. (**A**-**D**) Representative western blots and relative IP quantification (*bar graphs*) of IP against Myc-PUM1-WT, Myc-PUM1-T1035S (PRCA), or Myc-PUM1-R1147W (PADDAS) followed by immunoblotting for: (**A**) GST-AGO2, (**B**) GST-CNOT1, (**C**) GST-FMRP, and (**D**) GST-PUM1-WT (to test the dimerization of PUM1 proteins). Myc- and GST-tagged proteins were co-transfected in HEK293T cells in equal quantities (250ng each). The molecular weights were expressed in kilodaltons (kDa). The amount of protein pulled down compared to IP-PUM1 was quantified as $[IP^{X}/(Input^{X}/GAPDH^{X})]/[IP^{PUM1}/(Input^{PUM1}/GAPDH^{PUM1})]$, where X is the protein of interest. (**E**) qPCR analysis of validated PUM1-specific targets from PADDAS patient-derived fibroblasts (S1, blue bars) compared to three age- and sex-matched fibroblast control cell lines, and PRCA patient-derived lymphoblastoid cell lines (S2 and S3, orange bars) compared to the three age- and sex-matched lymphoblastoid control cell lines. (**F**) mRNA level quantification of PUM1 neuronal targets in common with FMRP, PUM2, AGO2, and RBFOX3 (**Figure 5E** and **Table S5**) in fibroblasts from subject 1 (PADDAS patient, R1147W) compared to the three age- and sex-matched control fibroblast lines (blue bars), and in lymphoblastoid cells from subjects 2 and 3 (PRCA patients, T1035S) compared to the three age- and sex-matched control lymphoblastoid cell lines (orange bars). For **E** and **F**, all data were normalized to *GAPDH* mRNA levels and experiments performed at least three times. Only genes expressed in both fibroblasts and lymphoblasts are represented here for a total of 10 for panel **E** and 55 for panel **F**. Data represent mean ± SEM. P values were calculated by two-tailed Student's t test. $*p < 0.05$, $**p < 0.01$, $***p < 0.001$.

SUPPLEMENTAL FIGURE LEGENDS

Figure S1. Immunoprecipitation (IP) antibody specificity against Pum1 from mouse brain and Pum1 interactor validation, related to Figure 1. (**A**) Pre-IP, IP, and post-IP against Pum1 and IgG from wild-type mouse brain show the specificity of the antibody used against Pum1. Pre-IP represents 1% from

the initial protein lysate as loading control while 10% of the protein lysate after IP-Pum1 was loaded as post-IP. The numbers on the right show molecular weight in kilodaltons (kDa). (**B**) Principal component analysis (PCA) of IP-Pum1 followed by mass spectrometry (MS) in WT adult mouse brains compared with IP against IgG; each dot represents two combined samples for a total of 6 samples processed by mass spectrometry. (**C**) Representative western blot of Rptor, Cad, Anapc1 and Fzr1 proteins pulled down by IP against Pum1 (used here as positive control) from WT mice. (**D**) Representative western blot of the reciprocal co-IPs against Anapc1, Fzr1, Rptor, and Cad. Each co-IP was immunoblotted against Pum1 and the pulled down protein used here as a reference protein to confirm the respective protein-protein interaction. For **C** and **D**, IP against IgG was used as negative control, and Input (1% from the initial protein lysate) as loading control. Molecular weights are expressed in kilodaltons (kDa) to the right. All the experiments were repeated at least four times. All mice were sacrificed at 10 weeks of age with an equal number or male and female.

Figure S2. Pum1 interactors differ by brain region, related to Figure 1. (**A**) Principal component analysis (PCA) of IP-Pum1 followed by mass spectrometry (MS) in cortex, hippocampus, and cerebellum from WT mice. IP against IgG was used as negative control. Each dot represents a total of 3 samples processed by MS for each brain region. (**B**) Pum1 interactome from cerebellum, hippocampus, cortex and the rest of the brain (i.e., excluding those three regions) showing all Pum1 putative interactors with a fold change > 1.5 (see also **Table S1**), for a total of 1,500 proteins. Node colors represent different brain regions or the overlap between two or more brain regions as noted. (**C**) After IP against Pum1 we immunoblotted for Pum1 (positive control), Anapc1, Cnot1 and Pum2. While Cnot1 and Anapc1 can be pulled down from all three brain regions, Pum2 can only be pulled down from cortex. For **A-C** we combined cerebellar and cortical tissues from eight wild-type mice (4 male and 4 female) for a total of 24 mice in triplicate for cerebellum and cortex, while for hippocampus we combined tissues from ten wild-type mice (5 female and 5 male) for a total of 30 mice in triplicate. All mice were 10 weeks of age. IP against IgG was used as negative control. Molecular protein weights are expressed in kilodaltons (kDa). (**D-F**) The three most enriched protein complexes among the Pum1 interactors for each brain region are shown in (**D**) for the anaphase promoting complex/cyclosome (APC/C); (**E**) for the mTOR pathway; (**F**) for RNA-silencing (RISC), CCR4-NOT, translation initiation and polyA binding. Edge colors (**D**, **E**, and **F**) represent a specific brain region: red for cortex, green for cerebellum, blue for hippocampus, and gray for proteins in common between two or more brain regions. (**G**) Western blot analysis at 10 weeks of age to evaluate Pum2 expression levels in eight different brain regions as well as whole brain. Pum2 is highly expressed in olfactory bulbs and amygdala, and expressed at similar levels in hippocampus, cerebellum, and cortex. HP: hippocampus; CB: cerebellum; CX: cortex; MB: midbrain; OB: olfactory bulbs; AM: amygdala; SN: substantia nigra pars compacta; BS: brain stem; WB: whole brain.

Figure S3. Immunoprecipitation (IP) against Pum1 and its interactors in wild-type and *Pum1*$^{-/-}$ mice with and without RNase treatment, related to Figure 3. (**A**) IP against Pum1 in *Pum1*$^{-/-}$ mouse demonstrates the complete absence of Pum1 and thus the specificity of the anti-Pum1 antibody. (**B-G**) Representative western blot of the proteins pulled down by (**B**) Pum2, (**C**) Fmrp, (**D**) Ago2, (**E**) Cnot1, (**F**) Mov10, and (**G**) Rbfox3 from wild-type (WT, *left panel*) and *Pum1*$^{-/-}$ (*right panel*) mouse brain without (*left panel*) and with (*right panel*) RNase treatment. IP against IgG was used as negative control, and Input (1% from the initial protein lysate) as loading control. Molecular weights at the right are in

kilodaltons (kDa). All the experiments were repeated at least four times. IP against IgG was used as negative control, and Input (1% from the initial protein lysate) as loading control. Equal numbers of male and female mice were sacrificed at 10 weeks of age.

Figure S4. Protein and mRNA quantification from whole brain in WT, *Pum1*$^{+/-}$ and *Pum1*$^{-/-}$ mice, related to Figure 4. (**A**) Representative western blot with relative quantifications of Pum1, Pum2, Fmrp, Ago2, Rbfox3, Cnot1, and Mov10 from the whole brain in WT, *Pum1*$^{+/-}$ and *Pum1*$^{-/-}$ mice. All data were normalized to Gapdh protein levels. The numbers on the right are the respective molecular weights expressed in kilodaltons (kDa). (**B**) mRNA level quantification by qPCR of *Pum1*, *Pum2*, *Fmrp*, *Ago2*, *Rbfox3*, *Cnot1*, and *Mov10* from whole brain in WT, *Pum1*$^{+/-}$ and *Pum1*$^{-/-}$ mice. Again, all data were normalized to *Gapdh* mRNA levels. All the experiments were conducted with equal number of male (at least 6 per genotype) and female (at least 6 per genotype) mice at 10 weeks of age, for a total of at least 12 mice per genotype, performed at least six times per genotype (data represent mean ± SEM). The *p* values were calculated by the Student's t test. $*p < 0.05$, $**p < 0.01$, $***p < 0.001$.

Figure S5. mRNA quantification of Pum1 interactors by brain region and sex and the 49 targets co-bound by at least eight dysregulated miRNAs in mouse cerebellum, related to Figure 4. (**A**) mRNA levels in cerebellum, hippocampus, and cortex in male and female for all the validated Pum1 interactors. The same number of mice were used here as in **Figure 4A-C** for a total of at least 9 mice per genotype and sex at 10 weeks of age. All data were normalized to *Gapdh* mRNA levels. All the experiments were performed at least six times (data represent mean ± SEM). (**B**) qPCR in cerebellum of male (*left*) and female (*right*) mice at 10 weeks of age for the 49 targets co-bound by at least eight dysregulated miRNAs (with minimum 20% change in expression) from **Figure 4E** and **Table S4**. All the experiments were performed in triplicate for three different biological replicates for both male and female (data represent mean ± SEM). The *p* values were calculated by two-tailed Student's t test. $*p < 0.05$, $**p < 0.01$, $***p < 0.001$.

Figure S6. Pum1, Pum2, Ago2, Fmrp, and Rbfox3 share a number of targets in the mouse brain, related to Figure 5. (**A**) Gene Set Enrichment Analysis (GSEA) of Pum1 HITS-CLIP data plotted against HITS-CLIP data from the negative controls (RNA binding proteins that did not show up in the Pum1 interactome: Ptpb2, Nova, Apc, and Mbnl2) reveals no significant enrichment. (**B-C**) Gene ontology analysis of the HITS-CLIP targets shared between Pum1, Pum2, Fmrp, Ago2, and Rbfox3 reveals enrichment for certain biological functions (**B**) and cellular localization (**C**). Only categories with FDR<0.05 and fold enrichment > 5 were plotted in **B** and **C**. (**D**) Venn diagram of miRNAs identified by Pum1, and Pum2 shows almost 100% overlap with the miRNAs pulled down by Fmrp HITS-CLIP. (**E**) GSEA of HITS-CLIP data normalized against gene expression in mouse brain at 3 weeks of age (see Methods) of Pum1, Pum2, Rbfox3, and Ago2 against Fmrp HITS-CLIP data ranked by normalized RPKM. (**F**) GSEA of HITS-CLIP data normalized against gene expression in mouse brain at 3 weeks of age (see Methods) of Mbnl2, Apc, Nova, and Ptpb2 plotted against Fmrp HITS-CLIP data ranked by normalized RPKM. Mbnl2, Ptpb2, Apc, and Nova were used as negative controls. (**G**) Fmrp, Pum2, Ago2, Rbfox3 shared targets, and targets of the four negative controls, plotted against Pum1 HITS-CLIP data ranked by normalized RPKM. (**H**) Pum1, Pum2, Ago2, Rbfox3 shared targets plotted against Fmrp HITS-CLIP data ranked by normalized RPKM. For all GSEA analyses the False Discovery Rate (FDR)

was provided by GSEA, ***FDR < 0.01. ES=Enrichment score (blue line). Note that lowest rank at max percentage ES indicates stronger targets in the rank.

Figure S7. PUM1 antibody efficiency for IP in fibroblast (PADDAS) and lymphoblastoid (PRCA) cell lines; mRNA quantification of PUM1 interactors in PADDAS and PRCA patient-derived cells; PUM1 stability assay, related to Figure 6. (**A-B**) Pre-IP, IP, and post-IP against PUM1 and IgG from (**A**) fibroblasts and (**B**) lymphoblastoid cells. In both cell lines we were able to pull down 100% of PUM1. Pre-IP represents 1% from the initial protein lysate as loading control, while 10% of the protein lysate was loaded as post-IP. Molecular weight at right in kilodaltons (kDa). (**C**) mRNA level quantification for all of the immunoblotted protein in **Figure 6C** (*PUM1*, *PUM2*, *FMR1*, *AGO2*, *CNOT1*, and *MOV10*) in PADDAS and PRCA patient-derived cell lines compared to their respective age-, sex-, and cell-type-matched controls. All data were normalized to *GAPDH* mRNA levels, and experiments performed at least six times. Data represent mean ± SEM. (**D**) PUM1 half-life in HEK293T at different time points, from zero (cycloheximide treatment) to 5h total upon Myc-PUM1-WT or Myc-PUM1-T1035S or Myc-PUM1-R1147W transfection. The half-life of the R1147W mutant is significantly shorter than that of WT and T1035S. All data were normalized to GAPDH and compared to time zero. The experiments were performed at least four times and the data represent mean ± SEM. The *p* values were calculated by two-tailed Student's t test. ***p* < 0.01, ***p < 0.001. (**E**) Representative western blots of IP with RNase treatment against Myc-PUM1-WT, Myc-PUM1-T1035S (PRCA), or Myc-PUM1-R1147W (PADDAS) followed by immunoblotting to test the dimerization between PUM1 proteins without the RNA. The numbers on the right are the respective molecular weights expressed in kilodaltons (kDa).

SUPPLEMENTAL TABLES AND LEGENDS

Table S1, to generate Figure 1A, S1 and S2. Pum1 mass spectrometry results from whole brain and three separate brain regions in 10-week-old mice. All the proteins have an FDR < 0.05, and only proteins with a Ratio LFQ-Pum1-WT/LFQ-IgG-WT > 1.5 are reported here.

Table S2, to generate Figure 1B. Gene Ontology analysis of Pum1 mass spectrometry from whole brain and the three brain regions. Only categories with fold enrichment of >1.5 and FDR<0.05 are shown.

Table S3, to generate Figure 4D. MicroRNA names and sequences with log2 fold change as represented in Figure 4D. PC = Predicted Candidate.

Table S4, to generate Figure 4E and S5B. Predicted target genes for all the differentially expressed miRNA (with at least 25% change) in cerebellum of male and female in wild-type and *Pum1*$^{-/-}$ mice at 10 weeks of age. The target genes tested have at least 8 co-bound miRNAs.

Table S5, to generate Figure 5, S6, and 7F. HITS-CLIP targets common to Pum1, Pum2, Ago2, Rbfox3, and Fmrp.

Table S6, to generate Figure S6D. microRNAs that overlap between Pum1, Pum2, and Fmrp HITS-CLIP data.

Table S7, to generate Figure S6E-H. RNAseq in mouse brain at 3 weeks of age.

Table S8. All primer sequences used in this study

RESOURCE AVAILABILITY

Lead Contact

Further information and requests for resources and reagents should be directed to and will be fulfilled by Vincenzo A. Gennarino (vag2138@cumc.columbia.edu).

Materials Availability

All unique reagents, cell lines and mouse models used in this manuscript are available upon request without restrictions. See Key Resource Table for details.

Data and Code Availability

No software was generated for this project. All software used in this study is publicly available and links are provided as appropriate in different sections of the Methods and Key Resource Table. Mass spectrometry raw data generated during this study are available at PRIDE Archive at https://www.ebi.ac.uk/pride/archive (with the accession number pending), and Gene Expression Omnibus (GEO) at https://www.ncbi.nlm.nih.gov/geo/ (with the accession number pending). Further information and requests for resources and reagents should be directed to and will be fulfilled by Vincenzo A. Gennarino (vag2138@cumc.columbia.edu).

EXPERIMENTAL MODEL AND SUBJECT DETAILS

Ethical statement and mouse strains. All animal procedures were approved by the Institutional Animal Care and Use Committee at Columbia University, New York under the protocol AC-AAAU8490. Mice were maintained on a 12-hr light, 12-hr dark cycle with regular chow and water ad libitum. Pum1 knock-out mice were generated as previously described (Chen et al., 2012). C57BL/6J wild-type mice were purchased from Jackson Laboratory and maintained as described above. For brain dissection, mice were anesthetized with isoflurane, and the brain rapidly removed from the skull and lysed in the appropriate buffer according to the experiment (see Methods Details).

HEK293T cell culture and maintenance. Human embryonic kidney immortalized 293T (HEK293T) cells were grown in DMEM (GenDepot, #CM002-320) supplemented with 10% of heat-inactivated fetal bovine serum (FBS [GenDepot, #F0901-050) and 1% penicillin/streptomycin (GenDepot, #CA005-010). All cells were incubated at 37 °C in a humidified chamber supplemented with 5% CO_2. HEK293T cells were later processed according to the needs of specific experiments (described below).

Patient-derived cell lines: fibroblasts and lymphoblasts. PADDAS and PRCA patient cell lines are the same as those reported previously (Gennarino et al., 2018). The consent form for each subject specifically allows for sharing of medical information and physical exam findings; the sharing of cell lines from the

PADDAS and PRCA subjects and the controls was approved under the Baylor College of Medicine IRB H-34578 and the Columbia University Medical Center IRB-AAAS7401 (Y01M00).

Primary fibroblasts from the *PUM1* PADDAS patient and the age- and sex-matched controls were generated as previously described (Gennarino et al., 2018). Briefly, cells were isolated from skin biopsies taken from the patient or age-matched controls using standard methodology (Barch and Association of Cytogenetic Technology, 1991) and placed in a transport medium (Ham's F10, Thermo Scientific, #11550043). The skin specimen was later removed from the transport medium using a sterile technique (in a Class II biohazard cabinet) and transferred to a sterile Petri dish where it was cut into small pieces (< 0.5 mm) using sterile scalpel blades. These pieces were transferred to the lower surface of a 25 cm^2 culture flask (6-8 pieces per flask) which had been pre-moistened with 1-2 mL of AmnioMAX Complete Medium (Thermo Scientific, #11269016) supplemented with 1% penicillin/streptomycin (GenDepot, #CA005-010). Cell cultures were maintained at 37 °C in a humidified incubator supplemented with 5% CO_2. When cell growth was observed around the edges of the tissue, usually 3 to 5 days later, 2 to 3 mL of AmnioMAX Complete Medium were added. Once growth was established and the tissue was anchored to the flask, another 8 mL of AmnioMAX Complete Medium was added. Thereafter, the medium was renewed every 3 to 4 days until ready for sub-culturing.

Lymphoblastoid cells from *PUM1* PRCA patients and the age- and sex-matched controls were generated as previously described (Gennarino et al., 2018). Briefly, lymphoblastoid suspension cell cultures were grown in RPMI 1640 medium (Invitrogen, #11875093) supplemented with 10% heat-inactivated fetal bovine serum (Atlanta Biological, Flowery Branch, #S11195H) and 1% penicillin/streptomycin (GenDepot, #CA005-010). Cell cultures were maintained at 37°C in a humidified incubator supplemented with 5% CO_2. Medium was renewed every 2 to 3 days.

METHODS DETAILS

Immunoprecipitation experiments using mouse brain tissue. Mouse brain tissues were gathered from an equal number of 10-week-old male and female mice as follows: whole brains from two mice; hippocampi from ten mice; cerebral cortices from eight mice; and cerebella from eight mice. Each grouping is considered one sample for one experiment. Samples were processed with a dounce homogenizer using a lysis buffer consisting of 200mM $NaCl_2$, 100mM $NaPO_4$, 20mM Hepes pH 7.4, 1% Triton X (which should disrupt all but the strongest protein-protein interactions) and complemented by 1X of Xpert Protease and 1X of Phosphatase Inhibitor Cocktail Solutions (GenDepot, #P3100-100, #P3200-020). Following homogenization, the samples were placed on ice for 15 minutes then centrifuged at 14,800 rpm at 4°C for 25 minutes to remove the debris from the supernatant. The supernatant was then moved to 1.5 ml tubes (Beckman microfuge tube #357448) and spun down in a Beckman ultra-centrifuge (Optima Max XP) at 4°C for 25 minutes at 44,000 rpm. 10% of the protein lysate was stored as input and only 1% was loaded for western blot. The protein extract was later divided into two aliquots, one for IP against the protein of interest (antibodies listed below) and the other for IP against IgG, and was then incubated with 30 µL of Dynabeads™ Protein G (Invitrogen, #10004D) and 5 µg of antibody overnight at 4°C on a rotisserie tube rotator. The next day, the beads were washed four times with the same lysis buffer used for IP and resuspended in 40µL of elution buffer (consisting of lysis buffer, NuPAGE 10X Reducing Agent [Invitrogen, #NP0009], NuPAGE LDS sample buffer at 1X final concentration [Invitrogen, #NP0007]) and boiled at 95°C for 10 minutes before the samples were loaded in the NuPAGE 4%–12% Bis-Tris Gels (Invitrogen, #NP0335BOX & #NP0336BOX) for further resolution and

western blot analysis.

For the IP with RNase treatment, the beads were resuspended in 400 µL of lysis buffer after the three final washes and divided into two separate 1.5 ml tubes of 200 µL each. To establish the dose required to remove all RNA, we tested different amounts of RNase I (Invitrogen, #EN0602) and found that 4 µL was enough to render RNA undetectable both by denaturing gel and cDNA amplification. The negative control was to go without RNase treatment; both were incubated at 37°C for 15 min on a rotisserie tube rotator. After incubation, all the samples were washed one last time with 500 µL of lysis buffer and then eluted in 20 µL of elution buffer. We used the same protocol for all the IP processed by mass spectrometry.

The antibodies used for IP were: goat α-PUM1 (Bethyl Laboratories, #A300-201A), rabbit α-PUM2 (Bethyl Laboratories, #A300-202A), rabbit α-FMRP (Abcam Cambridge, #ab17722), rabbit α-AGO2 (Abcam Cambridge, #ab32381), rabbit α-NeuN (Thermo Fisher Scientific, #PA5-37407), rabbit α-CNOT1 (Cell Signaling Technology, #44613), rabbit α-MOV10 (Bethyl Laboratories, #A301-571A), rabbit α-RAPTOR (Cell Signaling Technology, #2280), rabbit α-CAD (Bethyl Laboratories, #A301-374A), rabbit α-ANAPC1 (Bethyl Laboratories, #A301-653A), and rabbit α-FZR1 (Thermo Fisher Scientific, #PA5-85303).

N.B.: The reason the inputs are separated from the IPs and then collaged is because *in vivo* we load only 1% of the lysate, which we later run off the same blot of the IPs and expose the membrane to see either the input (which usually appears first) or the IPs (which for some of them appear with a longer exposure). This is common practice when working with *in vivo* tissues (De Maio et al., 2018) (Lee et al., 2008) (Rousseaux et al., 2018) (Di Grazia et al., 2021) (Jin et al., 2020) (Lee et al., 2020).

Immunoprecipitation experiments from HEK293T and patient-derived cell lines. HEK293T cells and patient-derived fibroblasts or lymphoblastoid cells were lysed by pipetting up and down with a 1000µl tip in a lysis buffer consisting of 200mM $NaCl_2$, 100mM $NaPO_4$, 20mM Hepes pH 7.4, 1% Triton X and complemented by 1X of Xpert Protease and 1X of Phosphatase Inhibitor Cocktail (GenDepot, #P3100-100, #P3200-020). The rest of the protocol is the same as described above for mouse brain tissue, except that we used 2.5 µg of primary antibody for IP.

Co-Immunoprecipitation in-gel digestion for mass spectrometry. Immunoprecipitated samples were separated on NuPAGE 4-12% gradient SDS-PAGE (Invitrogen, #NP0335BOX & #NP0336BOX) and stained with SimplyBlue (Invitrogen, #LC6060). Protein gel slices were excised and *in-gel* digestion performed as previously described (Shevchenko et al., 2006), with minor modifications. Gel slices were washed with 1:1 Acetonitrile and 100mM ammonium bicarbonate for 30 min then dehydrated with 100% acetonitrile for 10 min until shrunk. The excess acetonitrile was then removed and the slices dried in a speed-vacuum at room temperature for 10 minutes. Gel slices were reduced with 5 mM DTT for 30 min at 56ºC in an air thermostat, cooled down to room temperature, and alkylated with 11 mM IAA for 30 min with no light. Gel slices were then washed with 100 mM of ammonium bicarbonate and 100% acetonitrile for 10 min each. Excess acetonitrile was removed and dried in a speed-vacuum for 10 min at room temperature and the gel slices were re-hydrated in a solution of 25 ng/µl trypsin in 50 mM ammonium bicarbonate for 30 min on ice and digested overnight at 37 ºC in an air thermostat. Digested peptides were collected and further extracted from gel slices in extraction buffer (1:2 ratio by volume of 5% formic acid: acetonitrile) at high speed, shaking in an air thermostat. The supernatants from both

extractions were combined and dried in a speed-vacuum. Peptides were dissolved in 3% acetonitrile/0.1% formic acid.

Liquid chromatography with tandem mass spectrometry (LC-MS/MS). The Thermo Scientific Orbitrap Fusion Tribrid mass spectrometer was used for peptide tandem mass spectroscopy (MS/MS). Desalted peptides were injected in an EASY-Spray™ PepMap™ RSLC C18 50cm X 75cm ID column (Thermo Scientific) connected to the Orbitrap Fusion™ Tribrid™. Peptide elution and separation were achieved at a non-linear flow rate of 250 nl/min using a gradient of 5%-30% of buffer B (0.1% (v/v) formic acid, 100% acetonitrile) for 110 minutes, maintaining the temperature of the column at 50 °C during the entire experiment. Survey scans of peptide precursors are performed from 400 to 1500 *m/z* at 120K full width at half maximum (FWHM) resolution (at 200 *m/z*) with a 2 x 10^5 ion count target and a maximum injection time of 50 ms. The instrument was set to run in top speed mode with 3-second cycles for the survey and the MS/MS scans. After a survey scan, MS/MS was performed on the most abundant precursors, i.e., those exhibiting a charge state from 2 to 6 of greater than 5 x 10^3 intensity, by isolating them in the quadrupole at 1.6 Th. We used collision-induced dissociation (CID) with 35% collision energy and detected the resulting fragments with the rapid scan rate in the ion trap. The automatic gain control (AGC) target for MS/MS was set to 1 x 10^4 and the maximum injection time was limited to 35ms. The dynamic exclusion was set to 45s with a 10ppm mass tolerance around the precursor and its isotopes. Monoisotopic precursor selection was enabled.

LC-MS/MS data analysis. Raw mass spectrometric data were analyzed using the MaxQuant environment v.1.6.1.0 (Cox and Mann, 2008) and Andromeda for database searches (Cox et al., 2011) at default settings with a few modifications. The default was used for first search tolerance and main search tolerance (20 ppm and 6 ppm, respectively). MaxQuant was set up to search with the reference mouse proteome database downloaded from Uniprot (https://www.uniprot.org/proteomes/UP000000589). MaxQuant performed the search for trypsin digestion with up to 2 missed cleavages. Peptide, site and protein false discovery rates (FDR) were all set to 1% with a minimum of 1 peptide needed for identification; label-free quantitation (LFQ) was performed with a minimum ratio count of 1. The following modifications were used for protein quantification: oxidation of methionine (M), acetylation of the protein N-terminus, and deamination for asparagine or glutamine (NQ). Results obtained from MaxQuant were further analyzed using the Perseus statistical package (Tyanova et al., 2016) that is part of the MaxQuant distribution. Protein identifications were filtered for common contaminants. Proteins were considered for quantification only if they were found in at least two replicate groups. Significant alterations in protein abundance were determined by ANOVA with a threshold for significance of $P < 0.05$ (permutation-based FDR correction). Pum1 protein interactors were later considered if they were found in at least five out of six mass spec experiments for whole brain and in at least two out of three experiments for each respective brain region with a fold-change of >1.5 between LFQ-PUM1-WT and LFQ-IgG-WT (see **Table S1**).

Protein-protein interaction map. The protein-protein interaction map for the whole brain (**Figure 1A)** was generated by Cytoscape (https://cytoscape.org/) (Otasek et al., 2019) and the interactions among the Pum1 interactors were inferred from Corum (Giurgiu et al., 2019) and the Human Protein Atlas (Thul et al., 2017) by g:GOSt which is a package of g:Profiler (https://biit.cs.ut.ee/gprofiler/gost) (Raudvere et al.,

2019). The protein-protein interaction to generate the brain region-specific map (**Figure S2B**) was generated by Cytoscape.

Protein quantification and western blot analysis. Patient-derived lymphoblastoid, fibroblast cell lines, and control cell lines were collected at 6×10^6 cell confluence and processed for protein extraction. For mouse tissues, we processed either half brain (the other half was processed for RNA extraction, see below) or the entire hippocampus, cortex, or cerebellum for protein extraction. Mouse tissues or cell pellets were subsequently lysed with modified RIPA buffer consisting of 25 mM Tris-HCL, pH 7.6, 150 mM NaCl, 1.0% Tween 20, 1.0% sodium deoxycholate, 0.1% SDS, completed with 1X Xpert Protease and 1X Phosphatase Inhibitor Cocktail Solutions (GenDepot, #P3100-100 & #P3200-020). Cells were lysed by pipetting them up and down with a p1000 tip and then placed on ice for 20 min followed by centrifugation at 14,800 rpm at 4°C for 25 minutes. Mouse brain tissues were lysed starting from a 18G 1 ½" (Becton Dickson, #305196) and move down to 21G 1 ½" (Becton Dickson, #305167) and finally to 26G 1 ½" (Becton Dickson, #305111) syringe needles by pipetting them up and down until the lysate passed through the needle smoothly. Proteins were quantified by Pierce BCA Protein Assay Kit (Thermo Scientific, # PI23225) and the absorbance was measured by NanoDrop OneC (Thermo Scientific). Consequently, proteins were resolved by high resolution NuPAGE 4%–12% Bis-Tris Gel (Invitrogen, #NP0335BOX & #NP0336BOX) according to the manufacturer's instructions. All the blots were acquired on the G:BOX Chemi XX9 machine (Syngene; Frederick, MD) using GeneSys software 1.6.5.0. Gel exposures were determine by the software.

Antibodies used for all the western blot experiments were: goat α-PUM1 [1:2500, (Bethyl Laboratories, #A300-201A)], rabbit α-PUM1 [1:2000, (Abcam Cambridge, #ab92545)], rabbit α-PUM2 [1:2000, (Bethyl Laboratories, # A300-202A)], rabbit α-FMRP [1:1000, (Abcam Cambridge, #ab17722)], rabbit α-AGO2 [1:1000, (Abcam Cambridge, #ab32381)], rabbit α-NeuN (Rbfox3) [1:1000, (Thermo Scientific, #PA5-37407)], rabbit α-CNOT1 [1:1000, (Cell Signaling Technology, #44613)], rabbit α-MOV10 [1:2000, (Bethyl Laboratories, #A301-571A)], and mouse α-GAPDH [1:10000, (Millipore, #CB1001)].

RNA extraction and quantitative real-time PCR (qPCR). Human fibroblast, lymphoblastoid, and respective control cell lines were harvested at $6 \text{ X } 10^6$ confluence prior to RNA extraction. For mouse tissues, half of the whole brain (the other half was processed for protein extraction, see above) or the entire hippocampus, cortex, or cerebellum were processed for RNA extraction. The RNA was collected for both human cells, mouse brain and brain region tissues using the miRNeasy kit (QIAGEN, # 217004) according to the manufacturer's instructions. RNA was quantified using NanoDrop OneC (Thermo Fisher Scientific). cDNA was synthesized using Quantitect Reverse Transcription kit (QIAGEN, # 205313) starting from 1 µg of RNA. Quantitative RT-polymerase chain reaction (qRT-PCR) experiments were performed using the CFX96 Touch Real-Time PCR Detection System (Bio-Rad Laboratories, Hercules) with PowerUP SYBR Green Master Mix (Applied Biosystems, #A25743). Real-time PCR runs were analyzed using the comparative C_T method normalized against the housekeeping human gene *GAPDH* or mouse *Gapdh*, depending on the experiment (Vandesompele et al., 2002).

Protein stability assay. HEK293T cells were seeded in 12-well plates for 24h and then transfected with 125 ng of either *PUM1* WT or mutant cDNA and one of the interactors using the jetPRIME Transfection

Reagent (Polyplus transfection, #55-132) according to the manufacturer's protocol. After 24 h cells were treated with 0.1 mg/ml of cycloheximide (Fisher Scientific, #AAJ66004XF), which we considered time zero. Cells were later collected after 30min, 1h, 2h, 4h and 5h of treatment and processed for protein extraction and western blot analysis. Antibody: mouse α-Myc antibody [1:2000, (Cell Signaling Technologies, #2276)].

MicroRNA library construction and sequencing. Library preparation and microRNA sequencing was performed by LC Sciences according to the following criteria. Total RNA was extracted from cerebellum of WT and *Pum1*$^{-/-}$ male and female at 10 week of age in triplicate, for a total of 12 samples using the miRNeasy kit (QIAGEN, # 217004) according to the manufacturer's instructions. The total RNA quality and quantity were assessed with Bioanalyzer 2100 (Agilent Technologies, Santa Clara) with RIN number > 7.0. Approximately 1 µg of total RNA were used to prepare the small RNA library according to the protocol of TruSeq Small RNA Sample Prep Kits (Illumina, San Diego). Then the single-end sequencing 50bp was performed on an Illumina Hiseq 2500 at LC Sciences (Hangzhou, China) following the vendor's recommended protocol.

MicroRNA sequencing bioinformatic analysis. Raw reads were subjected to an in-house program, ACGT101-miR (LC Sciences, Houston) to remove adapter dimers, junk, low complexity, common RNA families (rRNA, tRNA, snRNA, snoRNA) and repeats. Subsequently, unique sequences of 18–26 nucleotides in length were mapped to specific species precursors in miRBase 22.0 (http://www.mirbase.org/) by BLAST search to identify known miRNAs and novel 3p- and 5p-derived miRNAs. Length variation at both 3' and 5' ends and one mismatch inside of the sequence were allowed in the alignment. The unique sequences mapping to specific species of mature miRNAs in hairpin arms were identified as known miRNAs. The unique sequences mapping to the other arm of known specific species precursor hairpins opposite the annotated mature miRNA-containing arm were considered to be novel 5p- or 3p-derived miRNA candidates. The remaining sequences were mapped to other selected species precursors (with the exclusion of specific species) in miRBase 22.0 by BLAST search, and the mapped pre-miRNAs were further BLASTed against the specific species genomes to determine their genomic locations. The last two were also defined as known miRNAs. The unmapped sequences were BLASTed against the specific genomes, and the hairpin RNA structures containing sequences were predicted from the flank 80 nt sequences using RNAfold software (http://rna.tbi.univie.ac.at/cgi-bin/RNAWebSuite/RNAfold.cgi). The criteria for secondary structure prediction were: (1) number of nucleotides in one bulge in stem (≤12), (2) number of base pairs in the stem region of the predicted hairpin (≥16), (3) cutoff of free energy (kCal/mol ≤-15), (4) length of hairpin (up and down stems + terminal loop ≥50), (5) length of hairpin loop (≤20), (6) number of nucleotides in one bulge in mature region (≤8), (7) number of biased errors in one bulge in mature region (≤4), (8) number of biased bulges in mature region (≤2), (9) number of errors in mature region (≤7), (10) number of base pairs in the mature region of the predicted hairpin (≥12), (11) percent of mature region in stem (≥80).

RNA sequencing. The Genomic and RNA Profiling Core at Baylor College of Medicine first conducted Sample Quality checks using the NanoDrop spectrophotometer and Agilent Bioanalyzer 2100. We then used Illumina TruSeq Stranded Total RNA library preparation protocol (p/n 15031048, revE, document #RS-122-9007) along with ThermoFisher's ERCC RNA Spike-In Control Mixes Protocol (publication

number 4455352, rev. D). Our process is as follows:

Illumina TruSeq stranded total RNA sample preparation protocol: Total RNA samples were normalized to 250ng each, based on picogreen quantitation, and ERCC RNA Spike-In Controls (p/n 4456739) were incorporated into each sample. Using the TruSeq Stranded Total RNA Library Prep Gold Kit (p/n RS-122-2301), samples then underwent ribosomal RNA reduction and subsequently fragmented and primed with random hexamers to produce first strand cDNA. During second strand cDNA synthesis, RNA templates were removed and replaced with cDNA strands containing dUTP. The ds-cDNA was then purified using Beckman Coulter AMPure XP beads (p/n A63881).

Library preparation: Libraries were created from the cDNA by attaching an adenosine to the 3' end and ligating unique adapters to the ends (for more information on this process, see below). The ligated products underwent 15 cycles of amplification and a final bead purification. The resulting libraries were quantitated using the NanoDrop spectrophotometer and fragment size assessed using the Agilent 2100 Bioanalyzer. A qPCR assay was performed on the libraries to determine the concentration of adapter ligated fragments using the Applied Biosystems ViiA 7 Quantitative PCR instrument and a KAPA Library Quant Kit (p/n KK4824). All samples were pooled equimolarly and re-quantitated by qPCR, and also re-assessed on the Bioanalyzer.

Cluster generation by bridge amplification: HiSeq 2500 HOM. Using the concentration from the ViiA7 qPCR machine above, 26pM of equimolarly pooled library was loaded onto three lanes of a high output v4 flowcell (Illumina p/n PE-401-4001) and amplified by bridge amplification using the Illumina cBot machine (cBot protocol: PE_HiSeq_Cluster_Kit_v4_cBot_recipe_v9.0). PhiX Control v3 adapter-ligated library (Illumina p/n FC-110-3001) is spiked-in at 2% by weight to ensure balanced diversity and to monitor clustering and sequencing performance. A paired-end 100 cycle run was used to sequence the flowcell on a HiSeq 2500 Sequencing System (Illumina p/n FC-401-4003). An average of 129 million read pairs per sample was sequenced.

End repair converts the overhangs caused by fragmentation into blunt or polished ends. The 3' to 5' exonuclease activity of the End Repair mix removes the 3' overhangs, and polymerase activity fills in the 5' overhangs.

Adenylation: a single 'A' nucleotide is added to the 3' ends of the blunt fragments.

Adapter ligation: an adapter is ligated to the 3' end of the DNA fragment with a corresponding 'T' nucleotide.

Absolute expression: The absolute gene expression was calculated as DESeq2-normalized counts as previously described (Love et al., 2014) (**Table S7**).

Samples: RNAseq was performed in triplicate from whole C57BL/6J mouse brains at 3 weeks of age.

Gene Set Enrichment Analysis (GSEA). GSEA was performed as previously described (Subramanian et al., 2005). The cumulative distribution function was conducted by performing 1000 random gene-set membership assignments. A nominal p-value < 0.01 and an FDR < 0.25 were used to assess the significance of the enrichment score (ES). HITS-CLIP data were obtained from the literature and were initially acquired as follows: Pum1 and Pum2 from neonatal murine brains (Zhang et al., 2017), Fmrp from cerebellum, cortex, and hippocampus together (Maurin et al., 2018), Ago2 from neocortex at embryonic day 13 (Chi et al., 2009), Rbfox3 from mouse brain (age not specified) (Weyn-Vanhentenryck et al., 2014), Nova from mouse brain (age not specified) (Zhang et al., 2010), Ptpb2 from neocortex at embryonic day 18.5 (Licatalosi et al., 2012), Mbnl2 from hippocampus at 8-12 weeks of age (Charizanis

et al., 2012), and Apc from mouse brain at embryonic day 14 (Preitner et al., 2014). For consistency all the HITS-CLIP data were ranked according to their RPKM.

For the normalized RPKM-GSEA analysis we performed RNAseq experiments (as described above), in triplicate, from WT C57BL/6 mouse brain at 3 weeks of age (we chose this age to be comparable to the other HITS-CLIP datasets) to infer the basal level of gene expression by DESeq2-normalized counts (see above). We then normalized the RPKM values by the DESeq2-normalized counts and repeated the GSEA enrichment analysis.

Gene ontology analyses. All gene ontology analyses were performed with David Gene Ontology (GO) and only categories with FDR<0.05 were considered. David GO for the Pum1 interactome considered the entire interactome as background. For GSEA HITS-CLIP targets shared among Pum1, Pum2, Fmrp, Ago2, and Rbfox3, we considered the entire set of all targetomes together as background.

Myc and GST cloning procedure with in vitro immunoprecipitation (IP) assays. Human *PUM1* full-length cDNA was amplified by PCR and subcloned in a pRK5 plasmid containing the Myc tag sequence (Addgene, pRK5-Myc-Parkin #17612) at the N-terminal by using SalI (New England Biolabs, # R3138S) and NotI (New England Biolabs, #R0189S) restriction enzymes to replace *Parkin* with *PUM1*. For GST, the human full-length *PUM1* cDNA was, again, subcloned first in the pRK5 plasmid containing the GST tag sequence (Addgene, pRK5-HA GST RagC wt, #19304) at the N-terminal by using SalI and NotI restriction enzymes to replace *RagC* with *PUM1*. Human *FMRP*, *AGO2* and *CNOT1*, full-length cDNA were cloned and contain the GST tag sequence at the N-terminal as described for GST-*PUM1*.

To introduce the T1035S or R1147W mutations we used the QuikChange II XL Multi Site-Directed Mutagenesis kit (Agilent Technologies, #200521). The primers for the single mutagenesis experiments were designed by QuikChange software (Stratagene, San Diego, https://www.genomics.agilent.com/primerDesignProgram.jsp).

For IP, HEK293T cells were seeded in 6-well plates for 24 h and then transfected with 250 ng of either WT or mutant PUM1 plasmid with one of the interactors using the jetPRIME Transfection Reagent (Polyplus transfection, #55-132) as per the manufacturer's protocol. pRK5-Myc empty plasmid (no cDNA) was used as a negative control. After 48 h, the cells were collected and processed for immunoprecipitation. Protein lysates were incubated overnight at 4°C with mouse α-Myc antibody (1:400, [Cell Signaling Technologies, #2276]) on a rotisserie tube rotator. The next day, the beads were washed four times with an IP lysis buffer and resuspended in 40 µL elution buffer (lysis buffer, NuPAGE 10X Reducing Agent [Invitrogen, #NP0009], NuPAGE LDS sample buffer 4X [Invitrogen, #NP0007]) and boiled at 95°C for 10 minutes before loading the samples in NuPAGE 4%–12% Bis-Tris Gels (Invitrogen, #NP0335BOX & #NP0336BOX) for further resolution and western blot analysis. Antibodies: mouse α-Myc antibody [1:2000, (Cell Signaling Technologies, #2276)], rabbit α-GST antibody [1:1000, (Cell Signaling Technologies, #2625)], mouse α-GAPDH [1:10000, (Millipore, #CB1001)].

Primers. For the qPCR analysis to unambiguously distinguish spliced cDNA from genomic DNA contamination, specific exon primers were designed to amplify across introns of the gene tested. The primers for all genes tested were designed with Primer3 (Koressaar and Remm, 2007; Untergasser et al., 2012). Cloning primers were manually designed to amplify the longest spliced gene isoform tested; if there was more than one isoform according to the UCSC Genome Browser (https://genome.ucsc.edu/), we

chose the longest. See **Table S8** for primer sequences.

QUANTIFICATION AND STATISTICAL ANALYSIS

Experimental Design

For protein and RNA quantification from patient-derived cell lines, we used values from at least six independent experiments with three biological replicates for each experiment. At every stage of the study, the experimenter was blinded to the identity of control and patient-derived cell lines. For example, for the data regarding both human patient-derived cell lines and mice, Experimenter #1 made a list of samples and controls to be tested, and Experimenter #2 randomized this list and re-labeled the tubes; Experimenter #2 was the only person with the key to identify the samples. These samples were then distributed to Experimenter #3 to culture the cells, then to Experimenter #1 to perform western blots and qRT-PCR, and lastly Experimenters #1 and #4 analyzed the data. Only then was the key applied to identify the samples. For mouse experiments, the experimenters were randomized and blinded as described above. The number of animals used and sex, and the specific statistical tests used, are indicated for each experiment in the figure legends. Sample size was based on previous experience using the same mice (Gennarino et al., 2015).

Software and statistical analysis. Statistical significance was analyzed using GraphPad Prism 8 (https://www.graphpad.com/ scientific-software/prism/) and Excel Software (Microsoft). All data are presented as mean ± SEM. Statistical details for each experiment can be found in the figures and the legends. The range of expression levels in qPCR was determined from at least six independent experiments with three biological replicates by calculating the standard deviation of the **Δ**Ct (Pfaffl, 2001). The range of expression levels in western blots was determined from at least six independent experiments with at least six biological replicates. P values were calculated by Student's T-test or analysis of variance with Tukey's post hoc analysis. For the IP and protein quantification in patient cell lines in **Figure 7**, we had only one PADDAS patient, so the six repeated experiments were technical replicates rather than biological replicates. We therefore calculated the statistical significance based on these technical replicates in comparison to the three biological replicates (i.e., healthy controls).

REFERENCES

Agarwal, V., Bell, G.W., Nam, J.W., and Bartel, D.P. (2015). Predicting effective microRNA target sites in mammalian mRNAs. Elife *4*.

Almeida, A., Bolanos, J.P., and Moreno, S. (2005). Cdh1/Hct1-APC is essential for the survival of postmitotic neurons. The Journal of Neuroscience: the Official Journal of the Society for Neuroscience *25*, 8115-8121.

Bah, M.G., Rodriguez, D., Cazeneuve, C., Mochel, F., Devos, D., Suppiej, A., Roubertie, A., Meunier, I., Gitiaux, C., Curie, A.*, et al.* (2020). Deciphering the natural history of SCA7 in children. Eur J Neurol *27*, 2267-2276.

Blewett, N.H., and Goldstrohm, A.C. (2012). A eukaryotic translation initiation factor 4E-binding protein promotes mRNA decapping and is required for PUF repression. Molecular and Cellular Biology *32*, 4181-4194.

Bonnemason-Carrere, P., Morice-Picard, F., Pennamen, P., Arveiler, B., Fergelot, P., Goizet, C., Hellegouarch, M., Lacombe, D., Plaisant, C., Raclet, V.*, et al.* (2019). PADDAS syndrome associated

with hair dysplasia caused by a de novo missense variant of PUM1. American Journal of Medical Genetics Part A *179*, 1030-1033.
Charizanis, K., Lee, K.Y., Batra, R., Goodwin, M., Zhang, C., Yuan, Y., Shiue, L., Cline, M., Scotti, M.M., Xia, G.*, et al.* (2012). Muscleblind-like 2-mediated alternative splicing in the developing brain and dysregulation in myotonic dystrophy. Neuron *75*, 437-450.
Chartier-Harlin, M.C., Kachergus, J., Roumier, C., Mouroux, V., Douay, X., Lincoln, S., Levecque, C., Larvor, L., Andrieux, J., Hulihan, M.*, et al.* (2004). Alpha-synuclein locus duplication as a cause of familial Parkinson's disease. Lancet *364*, 1167-1169.
Chen, D., Zheng, W., Lin, A., Uyhazi, K., Zhao, H., and Lin, H. (2012). Pumilio 1 suppresses multiple activators of p53 to safeguard spermatogenesis. Current Biology:CB *22*, 420-425.
Chi, S.W., Zang, J.B., Mele, A., and Darnell, R.B. (2009). Argonaute HITS-CLIP decodes microRNA-mRNA interaction maps. Nature *460*, 479-486.
Conboy, J.G. (2017). Developmental regulation of RNA processing by Rbfox proteins. Wiley Interdisciplinary Reviews RNA *8*.
Cox, J., and Mann, M. (2008). MaxQuant enables high peptide identification rates, individualized p.p.b.-range mass accuracies and proteome-wide protein quantification. Nature Biotechnology *26*, 1367-1372.
Cox, J., Neuhauser, N., Michalski, A., Scheltema, R.A., Olsen, J.V., and Mann, M. (2011). Andromeda: a peptide search engine integrated into the MaxQuant environment. J Proteome Res *10*, 1794-1805.
Darnell, J.C., and Richter, J.D. (2012). Cytoplasmic RNA-binding proteins and the control of complex brain function. Cold Spring Harb Perspect Biol *4*, a012344.
Dassi, E. (2017). Handshakes and Fights: The Regulatory Interplay of RNA-Binding Proteins. Front Mol Biosci *4*, 67.
De Maio, A., Yalamanchili, H.K., Adamski, C.J., Gennarino, V.A., Liu, Z., Qin, J., Jung, S.Y., Richman, R., Orr, H., and Zoghbi, H.Y. (2018). RBM17 Interacts with U2SURP and CHERP to Regulate Expression and Splicing of RNA-Processing Proteins. Cell Reports *25*, 726-736 e727.
Di Grazia, A., Marafini, I., Pedini, G., Di Fusco, D., Laudisi, F., Dinallo, V., Rosina, E., Stolfi, C., Franze, E., Sileri, P.*, et al.* (2021). The Fragile X Mental Retardation Protein Regulates RIPK1 and Colorectal Cancer Resistance to Necroptosis. Cell Mol Gastroenterol Hepatol *11*, 639-658.
Edwards, T.A., Pyle, S.E., Wharton, R.P., and Aggarwal, A.K. (2001). Structure of Pumilio reveals similarity between RNA and peptide binding motifs. Cell *105*, 281-289.
Enwerem, III, Elrod, N.D., Chang, C.T., Lin, A., Ji, P., Bohn, J.A., Levdansky, Y., Wagner, E.J., Valkov, E., and Goldstrohm, A. (2021). Human Pumilio proteins directly bind the CCR4-NOT deadenylase complex to regulate the transcriptome. RNA.
Friend, K., Campbell, Z.T., Cooke, A., Kroll-Conner, P., Wickens, M.P., and Kimble, J. (2012). A conserved PUF-Ago-eEF1A complex attenuates translation elongation. Nature Structural & Molecular Biology *19*, 176-183.
Fuentes, N., Roy, A., Mishra, V., Cabello, N., and Silveyra, P. (2018). Sex-specific microRNA expression networks in an acute mouse model of ozone-induced lung inflammation. Biol Sex Differ *9*, 18.
Gehman, L.T., Meera, P., Stoilov, P., Shiue, L., O'Brien, J.E., Meisler, M.H., Ares, M., Jr., Otis, T.S., and Black, D.L. (2012). The splicing regulator Rbfox2 is required for both cerebellar development and mature motor function. Genes & Development *26*, 445-460.
Gennarino, V.A., D'Angelo, G., Dharmalingam, G., Fernandez, S., Russolillo, G., Sanges, R., Mutarelli, M., Belcastro, V., Ballabio, A., Verde, P.*, et al.* (2012). Identification of microRNA-regulated gene networks by expression analysis of target genes. Genome Research *22*, 1163-1172.
Gennarino, V.A., Palmer, E.E., McDonell, L.M., Wang, L., Adamski, C.J., Koire, A., See, L., Chen, C.A., Schaaf, C.P., Rosenfeld, J.A.*, et al.* (2018). A Mild PUM1 Mutation Is Associated with Adult-Onset Ataxia, whereas Haploinsufficiency Causes Developmental Delay and Seizures. Cell *172*, 924-936 e911.

Gennarino, V.A., Singh, R.K., White, J.J., De Maio, A., Han, K., Kim, J.Y., Jafar-Nejad, P., di Ronza, A., Kang, H., Sayegh, L.S., *et al.* (2015). Pumilio1 haploinsufficiency leads to SCA1-like neurodegeneration by increasing wild-type Ataxin1 levels. Cell *160*, 1087-1098.
Gieffers, C., Peters, B.H., Kramer, E.R., Dotti, C.G., and Peters, J.M. (1999). Expression of the CDH1-associated form of the anaphase-promoting complex in postmitotic neurons. Proc Natl Acad Sci U S A *96*, 11317-11322.
Giurgiu, M., Reinhard, J., Brauner, B., Dunger-Kaltenbach, I., Fobo, G., Frishman, G., Montrone, C., and Ruepp, A. (2019). CORUM: the comprehensive resource of mammalian protein complexes-2019. Nucleic Acids Research *47*, D559-D563.
Goldstrohm, A.C., Hall, T.M.T., and McKenney, K.M. (2018). Post-transcriptional Regulatory Functions of Mammalian Pumilio Proteins. Trends in Genetics:TIG *34*, 972-990.
Hentze, M.W., Castello, A., Schwarzl, T., and Preiss, T. (2018). A brave new world of RNA-binding proteins. Nature Reviews Molecular Cell Biology *19*, 327-341.
Imaizumi, T., Mogami, Y., Okamoto, N., Yamamoto-Shimojima, K., and Yamamoto, T. (2019). De novo 1p35.2 microdeletion including PUM1 identified in a patient with sporadic West syndrome. Congenit Anom (Kyoto) *59*, 193-194.
Jin, Z., Feng, H., Liang, J., Jing, X., Zhao, Q., Zhan, L., Shen, B., Cheng, X., Su, L., and Qiu, W. (2020). FGFR3 big up tri, open7-9 promotes tumor progression via the phosphorylation and destabilization of ten-eleven translocation-2 in human hepatocellular carcinoma. Cell Death Dis *11*, 903.
Kedde, M., van Kouwenhove, M., Zwart, W., Oude Vrielink, J.A., Elkon, R., and Agami, R. (2010). A Pumilio-induced RNA structure switch in p27-3' UTR controls miR-221 and miR-222 accessibility. Nature Cell Biology *12*, 1014-1020.
Keene, J.D. (2007). RNA regulons: coordination of post-transcriptional events. Nature Reviews Genetics *8*, 533-543.
Kenny, P.J., Kim, M., Skariah, G., Nielsen, J., Lannom, M.C., and Ceman, S. (2020). The FMRP-MOV10 complex: a translational regulatory switch modulated by G-Quadruplexes. Nucleic Acids Research *48*, 862-878.
Kenny, P.J., Zhou, H., Kim, M., Skariah, G., Khetani, R.S., Drnevich, J., Arcila, M.L., Kosik, K.S., and Ceman, S. (2014). MOV10 and FMRP regulate AGO2 association with microRNA recognition elements. Cell Reports *9*, 1729-1741.
Khalil, B., Morderer, D., Price, P.L., Liu, F., and Rossoll, W. (2018). mRNP assembly, axonal transport, and local translation in neurodegenerative diseases. Brain Res *1693*, 75-91.
Kim, K., Hessl, D., Randol, J.L., Espinal, G.M., Schneider, A., Protic, D., Aydin, E.Y., Hagerman, R.J., and Hagerman, P.J. (2019). Association between IQ and FMR1 protein (FMRP) across the spectrum of CGG repeat expansions. PloS One *14*, e0226811.
Koressaar, T., and Remm, M. (2007). Enhancements and modifications of primer design program Primer3. Bioinformatics *23*, 1289-1291.
Lai, K.L., Liao, Y.C., Tsai, P.C., Hsiao, C.T., Soong, B.W., and Lee, Y.C. (2019). Investigating PUM1 mutations in a Taiwanese cohort with cerebellar ataxia. Parkinsonism Relat Disord *66*, 220-223.
Lee, E.J., Seo, E., Kim, J.W., Nam, S.A., Lee, J.Y., Jun, J., Oh, S., Park, M., Jho, E.H., Yoo, K.H., *et al.* (2020). TAZ/Wnt-beta-catenin/c-MYC axis regulates cystogenesis in polycystic kidney disease. Proc Natl Acad Sci U S A *117*, 29001-29012.
Lee, J.T., Wheeler, T.C., Li, L., and Chin, L.S. (2008). Ubiquitination of alpha-synuclein by Siah-1 promotes alpha-synuclein aggregation and apoptotic cell death. Human Molecular Genetics *17*, 906-917.
Leeb, M., Dietmann, S., Paramor, M., Niwa, H., and Smith, A. (2014). Genetic exploration of the exit from self-renewal using haploid embryonic stem cells. Cell Stem Cell *14*, 385-393.

Licatalosi, D.D., Yano, M., Fak, J.J., Mele, A., Grabinski, S.E., Zhang, C., and Darnell, R.B. (2012). Ptbp2 represses adult-specific splicing to regulate the generation of neuronal precursors in the embryonic brain. Genes & Development *26*, 1626-1642.

Lin, H., and Spradling, A.C. (1997). A novel group of pumilio mutations affects the asymmetric division of germline stem cells in the Drosophila ovary. Development *124*, 2463-2476.

Liu, G.Y., and Sabatini, D.M. (2020). mTOR at the nexus of nutrition, growth, ageing and disease. Nature Reviews Molecular Cell Biology *21*, 183-203.

Love, M.I., Huber, W., and Anders, S. (2014). Moderated estimation of fold change and dispersion for RNA-seq data with DESeq2. Genome Biology *15*, 550.

Lukong, K.E., Chang, K.W., Khandjian, E.W., and Richard, S. (2008). RNA-binding proteins in human genetic disease. Trends in genetics: TIG *24*, 416-425.

Mandelboum, S., Manber, Z., Elroy-Stein, O., and Elkon, R. (2019). Recurrent functional misinterpretation of RNA-seq data caused by sample-specific gene length bias. PLoS Biol *17*, e3000481.

Mauger, O., Lemoine, F., and Scheiffele, P. (2016). Targeted Intron Retention and Excision for Rapid Gene Regulation in Response to Neuronal Activity. Neuron *92*, 1266-1278.

Maurin, T., Lebrigand, K., Castagnola, S., Paquet, A., Jarjat, M., Popa, A., Grossi, M., Rage, F., and Bardoni, B. (2018). HITS-CLIP in various brain areas reveals new targets and new modalities of RNA binding by fragile X mental retardation protein. Nucleic Acids Research *46*, 6344-6355.

McCabe, M.P., Cullen, E.R., Barrows, C.M., Shore, A.N., Tooke, K.I., Laprade, K.A., Stafford, J.M., and Weston, M.C. (2020). Genetic inactivation of mTORC1 or mTORC2 in neurons reveals distinct functions in glutamatergic synaptic transmission. Elife *9*.

Miles, W.O., Tschop, K., Herr, A., Ji, J.Y., and Dyson, N.J. (2012). Pumilio facilitates miRNA regulation of the E2F3 oncogene. Genes & Development *26*, 356-368.

Orr, H.T., and Zoghbi, H.Y. (2007). Trinucleotide repeat disorders. Annual Review of Neuroscience *30*, 575-621.

Otasek, D., Morris, J.H., Boucas, J., Pico, A.R., and Demchak, B. (2019). Cytoscape Automation: empowering workflow-based network analysis. Genome Biology *20*, 185.

Pfaffl, M.W. (2001). A new mathematical model for relative quantification in real-time RT-PCR. Nucleic Acids Research *29*, e45.

Preitner, N., Quan, J., Nowakowski, D.W., Hancock, M.L., Shi, J., Tcherkezian, J., Young-Pearse, T.L., and Flanagan, J.G. (2014). APC is an RNA-binding protein, and its interactome provides a link to neural development and microtubule assembly. Cell *158*, 368-382.

Qiu, C., Dutcher, R.C., Porter, D.F., Arava, Y., Wickens, M., and Hall, T.M.T. (2019). Distinct RNA-binding modules in a single PUF protein cooperate to determine RNA specificity. Nucleic Acids Research *47*, 8770-8784.

Raudvere, U., Kolberg, L., Kuzmin, I., Arak, T., Adler, P., Peterson, H., and Vilo, J. (2019). g:Profiler: a web server for functional enrichment analysis and conversions of gene lists (2019 update). Nucleic Acids Research *47*, W191-W198.

Ravanidis, S., Kattan, F.G., and Doxakis, E. (2018). Unraveling the Pathways to Neuronal Homeostasis and Disease: Mechanistic Insights into the Role of RNA-Binding Proteins and Associated Factors. Int J Mol Sci *19*.

Rousseaux, M.W.C., Tschumperlin, T., Lu, H.C., Lackey, E.P., Bondar, V.V., Wan, Y.W., Tan, Q., Adamski, C.J., Friedrich, J., Twaroski, K.*, et al.* (2018). ATXN1-CIC Complex Is the Primary Driver of Cerebellar Pathology in Spinocerebellar Ataxia Type 1 through a Gain-of-Function Mechanism. Neuron *97*, 1235-1243 e1235.

Rovelet-Lecrux, A., Hannequin, D., Raux, G., Le Meur, N., Laquerriere, A., Vital, A., Dumanchin, C., Feuillette, S., Brice, A., Vercelletto, M.*, et al.* (2006). APP locus duplication causes autosomal

dominant early-onset Alzheimer disease with cerebral amyloid angiopathy. Nature Genetics *38*, 24-26.
Salcedo-Arellano, M.J., Dufour, B., McLennan, Y., Martinez-Cerdeno, V., and Hagerman, R. (2020). Fragile X syndrome and associated disorders: Clinical aspects and pathology. Neurobiology of Disease *136*, 104740.
Sancak, Y., Peterson, T.R., Shaul, Y.D., Lindquist, R.A., Thoreen, C.C., Bar-Peled, L., and Sabatini, D.M. (2008). The Rag GTPases bind raptor and mediate amino acid signaling to mTORC1. Science *320*, 1496-1501.
Sandweiss, A.J., Brandt, V.L., and Zoghbi, H.Y. (2020). Advances in understanding of Rett syndrome and MECP2 duplication syndrome: prospects for future therapies. Lancet Neurol *19*, 689-698.
Shah, S., Molinaro, G., Liu, B., Wang, R., Huber, K.M., and Ritcher, J.D. (2020). FMRP Control of Ribosome Translocation Promotes Chromatin Modifications and Alternative Splicing of Neuronal Genes Linked to Autism. Cell Reports *30*.
Shevchenko, A., Tomas, H., Havlis, J., Olsen, J.V., and Mann, M. (2006). In-gel digestion for mass spectrometric characterization of proteins and proteomes. Nature Protocols *1*, 2856-2860.
Singh, K., Gaur, P., and Prasad, S. (2007). Fragile x mental retardation (Fmr-1) gene expression is down regulated in brain of mice during aging. Mol Biol Rep *34*, 173-181.
Singh, K., and Prasad, S. (2008). Differential expression of Fmr-1 mRNA and FMRP in female mice brain during aging. Mol Biol Rep *35*, 677-684.
Sivakumar, S., and Gorbsky, G.J. (2015). Spatiotemporal regulation of the anaphase-promoting complex in mitosis. Nature reviews Molecular Cell Biology *16*, 82-94.
Smidak, R., Sialana, F.J., Kristofova, M., Stojanovic, T., Rajcic, D., Malikovic, J., Feyissa, D.D., Korz, V., Hoeger, H., Wackerlig, J.*, et al.* (2017). Reduced Levels of the Synaptic Functional Regulator FMRP in Dentate Gyrus of the Aging Sprague-Dawley Rat. Front Aging Neurosci *9*, 384.
Sternburg, E.L., Estep, J.A., Nguyen, D.K., Li, Y., and Karginov, F.V. (2018). Antagonistic and cooperative AGO2-PUM interactions in regulating mRNAs. Sci Rep *8*, 15316.
Subramanian, A., Tamayo, P., Mootha, V.K., Mukherjee, S., Ebert, B.L., Gillette, M.A., Paulovich, A., Pomeroy, S.L., Golub, T.R., Lander, E.S.*, et al.* (2005). Gene set enrichment analysis: a knowledge-based approach for interpreting genome-wide expression profiles. Proc Natl Acad Sci U S A *102*, 15545-15550.
Takeguchi, R., Takahashi, S., Kuroda, M., Tanaka, R., Suzuki, N., Tomonoh, Y., Ihara, Y., Sugiyama, N., and Itoh, M. (2020). MeCP2_e2 partially compensates for lack of MeCP2_e1: A male case of Rett syndrome. Mol Genet Genomic Med *8*, e1088.
Tan, Q., and Zoghbi, H.Y. (2019). Mouse models as a tool for discovering new neurological diseases. Neurobiol Learn Mem *165*, 106902.
Temme, C., Simonelig, M., and Wahle, E. (2014). Deadenylation of mRNA by the CCR4-NOT complex in Drosophila: molecular and developmental aspects. Front Genet *5*, 143.
Tereshchenko, A., Magnotta, V., Epping, E., Mathews, K., Espe-Pfeifer, P., Martin, E., Dawson, J., Duan, W., and Nopoulos, P. (2019). Brain structure in juvenile-onset Huntington disease. Neurology *92*, e1939-e1947.
Thul, P.J., Akesson, L., Wiking, M., Mahdessian, D., Geladaki, A., Ait Blal, H., Alm, T., Asplund, A., Bjork, L., Breckels, L.M.*, et al.* (2017). A subcellular map of the human proteome. Science *356*.
Tyanova, S., Temu, T., Sinitcyn, P., Carlson, A., Hein, M.Y., Geiger, T., Mann, M., and Cox, J. (2016). The Perseus computational platform for comprehensive analysis of (prote)omics data. Nat Methods *13*, 731-740.
Untergasser, A., Cutcutache, I., Koressaar, T., Ye, J., Faircloth, B.C., Remm, M., and Rozen, S.G. (2012). Primer3--new capabilities and interfaces. Nucleic Acids Research *40*, e115.

Van Etten, J., Schagat, T.L., Hrit, J., Weidmann, C.A., Brumbaugh, J., Coon, J.J., and Goldstrohm, A.C. (2012). Human Pumilio proteins recruit multiple deadenylases to efficiently repress messenger RNAs. The Journal of Biological Chemistry *287*, 36370-36383.

Vandesompele, J., De Preter, K., Pattyn, F., Poppe, B., Van Roy, N., De Paepe, A., and Speleman, F. (2002). Accurate normalization of real-time quantitative RT-PCR data by geometric averaging of multiple internal control genes. Genome Biology *3*, RESEARCH0034.

Wamsley, B., Jaglin, X.H., Favuzzi, E., Quattrocolo, G., Nigro, M.J., Yusuf, N., Khodadadi-Jamayran, A., Rudy, B., and Fishell, G. (2018). Rbfox1 Mediates Cell-type-Specific Splicing in Cortical Interneurons. Neuron *100*, 846-859 e847.

Wang, X., Zamore, P.D., and Hall, T.M. (2001). Crystal structure of a Pumilio homology domain. Molecular Cell *7*, 855-865.

Warnefors, M., Mossinger, K., Halbert, J., Studer, T., VandeBerg, J.L., Lindgren, I., Fallahshahroudi, A., Jensen, P., and Kaessmann, H. (2017). Sex-biased microRNA expression in mammals and birds reveals underlying regulatory mechanisms and a role in dosage compensation. Genome Research *27*, 1961-1973.

Weidmann, C.A., Raynard, N.A., Blewett, N.H., Van Etten, J., and Goldstrohm, A.C. (2014). The RNA binding domain of Pumilio antagonizes poly-adenosine binding protein and accelerates deadenylation. RNA *20*, 1298-1319.

Weyn-Vanhentenryck, S.M., Mele, A., Yan, Q., Sun, S., Farny, N., Zhang, Z., Xue, C., Herre, M., Silver, P.A., Zhang, M.Q*., et al.* (2014). HITS-CLIP and integrative modeling define the Rbfox splicing-regulatory network linked to brain development and autism. Cell Reports *6*, 1139-1152.

Zamore, P.D., Bartel, D.P., Lehmann, R., and Williamson, J.R. (1999). The PUMILIO-RNA interaction: a single RNA-binding domain monomer recognizes a bipartite target sequence. Biochemistry *38*, 596-604.

Zamore, P.D., Williamson, J.R., and Lehmann, R. (1997). The Pumilio protein binds RNA through a conserved domain that defines a new class of RNA-binding proteins. RNA *3*, 1421-1433.

Zhang, C., Frias, M.A., Mele, A., Ruggiu, M., Eom, T., Marney, C.B., Wang, H., Licatalosi, D.D., Fak, J.J., and Darnell, R.B. (2010). Integrative modeling defines the Nova splicing-regulatory network and its combinatorial controls. Science *329*, 439-443.

Zhang, M., Chen, D., Xia, J., Han, W., Cui, X., Neuenkirchen, N., Hermes, G., Sestan, N., and Lin, H. (2017). Post-transcriptional regulation of mouse neurogenesis by Pumilio proteins. Genes & Development *31*, 1354-1369.

Zhang, Y., Gao, J., Chung, K.K., Huang, H., Dawson, V.L., and Dawson, T.M. (2000). Parkin functions as an E2-dependent ubiquitin- protein ligase and promotes the degradation of the synaptic vesicle-associated protein, CDCrel-1. Proc Natl Acad Sci U S A *97*, 13354-13359.

Zoghbi, H.Y., and Bear, M.F. (2012). Synaptic dysfunction in neurodevelopmental disorders associated with autism and intellectual disabilities. Cold Spring Harb Perspect Biol *4*.

Zylka, M.J., Simon, J.M., and Philpot, B.D. (2015). Gene length matters in neurons. Neuron *86*, 353-355.

Figure 1, Botta et al.

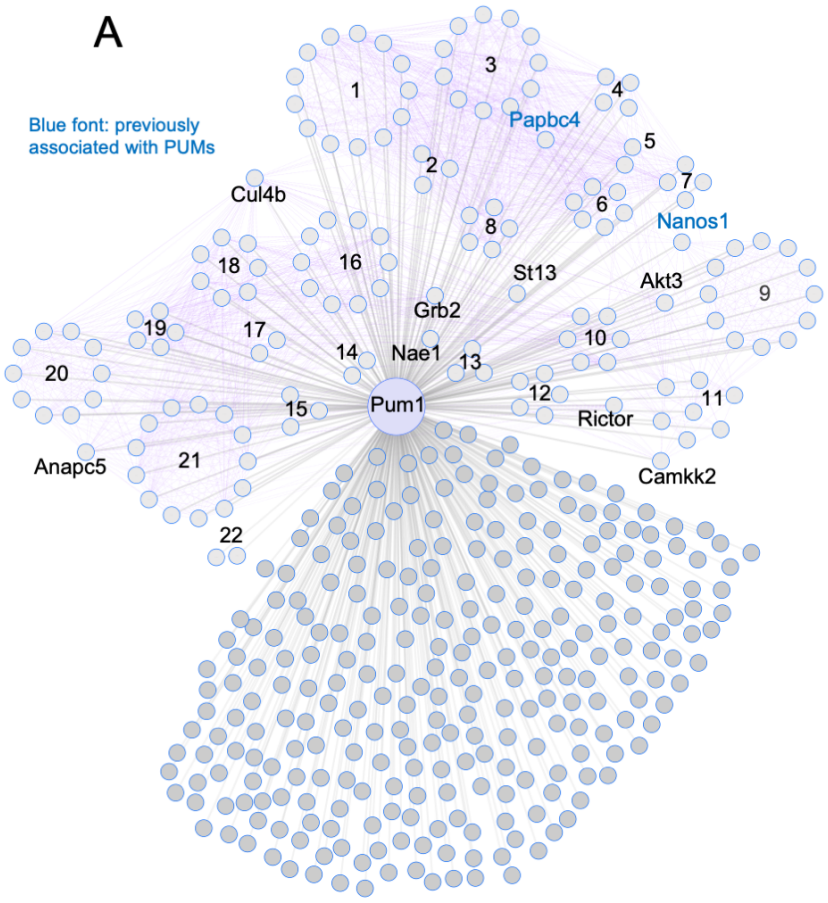

Cluster 1
Hnrnpul1
Dhx15
Eftud2
Wdr20
Usp46
Wdr48
Rbm39
Sf3b3
Srrt
Acin1
Snrnp200
Ddx3x

Cluster 2
Aff4
Mllt3
Mllt1

Cluster 3
Eif3f
Eif2s1
Eif5
Ctif
Eif4a3
Eif2s3x
Eif2s3y
Eif4g3
Eif2s2
Eif3b
Eif3l

Cluster 4
Thrap3
Upf1
Elavl4
Etf1

Cluster 5
Hnrnpa0
Hnrnpl

Cluster 6
Ssbp2
Khdrbs1
D1Pas1
Ssb
Ssbp3
Snd1

Cluster 7
Paip1
Rangap1
Rae1
Csde1

Cluster 8
Ago2
Fmrp
Rbfox3
Cnot1
Pum2

Cluster 9
Brsk2
Snx2
Pck2
Atg7
Pex5l
Fga
Fgb
Fgg
Rab11fip5
Madd
Stxbp5l
Snx4

Cluster 10
Matr3
Pfkp
Pfkm
Pspc1
Pfkl
Pfkfb2

Cluster 11
Pten
Tsc1
Tsc2
Rptor
Cad
Lrpprc
Lppr4

Cluster 12
Clip2
Rhob
Rhot1
Clasp1
Camk1d

Cluster 13
Prmt5
Rpl24
Tuba1a

Cluster 14
Kcna1
Kcna2

Cluster 15
Smarce1
Actbl2
Actl6b

Cluster 16
Cul4a
Rnf14
Uba3
Uba5
Trim32
Cul1
Pja1
Rlim
Mycbp2

Cluster 17
Ttc7b
Pi4ka

Cluster 18
Elp3
Pikr4
Ruvbl1
Prpsap2
Papss1
Zyg11b
Eea1

Cluster 19
Rbbp7
Hdac2
Kdm1a
Ogt
Zmym2

Cluster 20
Ppp1r21
Ppp1r16b
Ppp2r5c
Ppp6r2
Ppp1r12c
Ppp1r12b
Ppp1r12a
Ppp6r1
Ppp1cb
Ppp2r5d

Cluster 21
Fzr1
Sh3kbp1
Anapc1
Anapc2
Anapc7
Anapc10
Cdc16
Cdc23
Cdc27
Dnaja1
Znf281
Cep97

Cluster 22
Osbpl1
Osbpl8

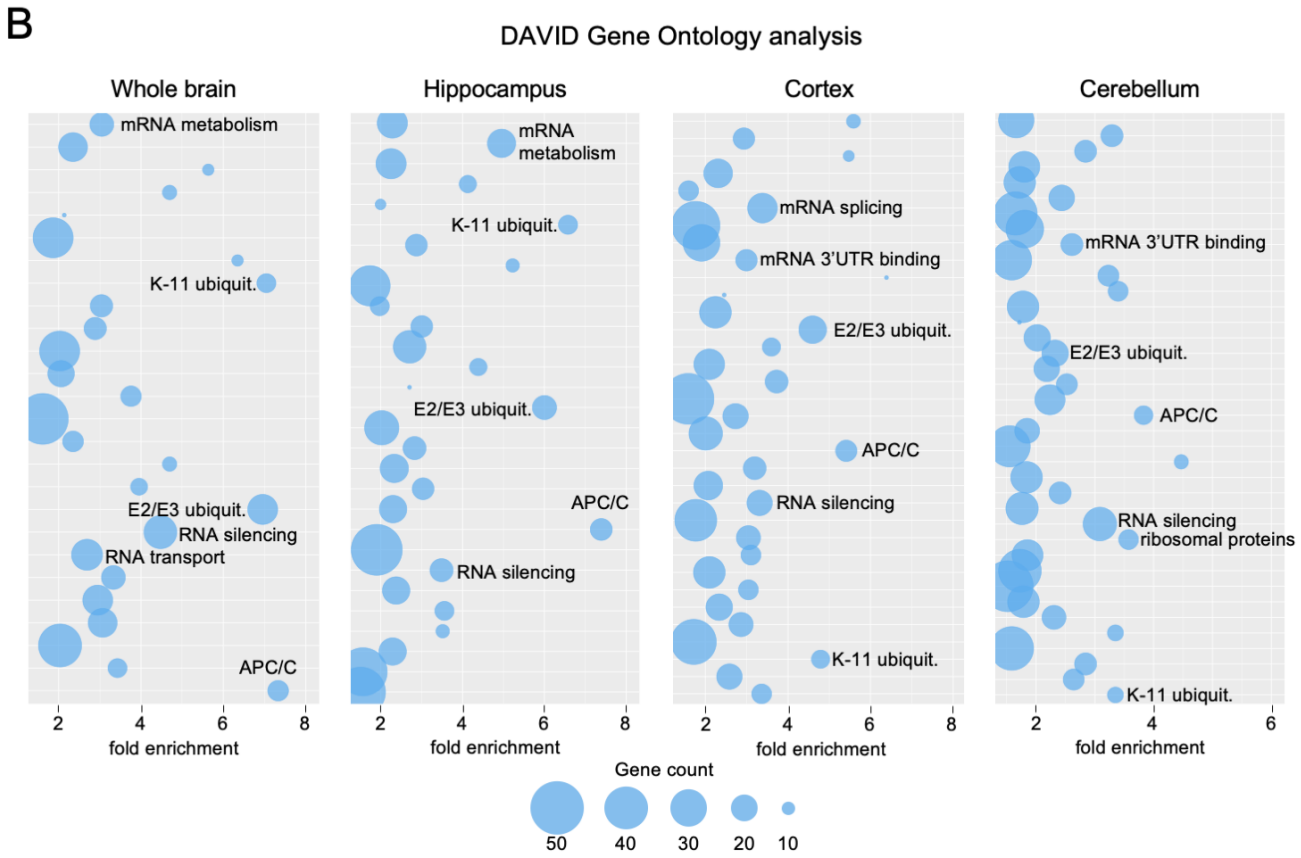

Figure 2, Botta et al.

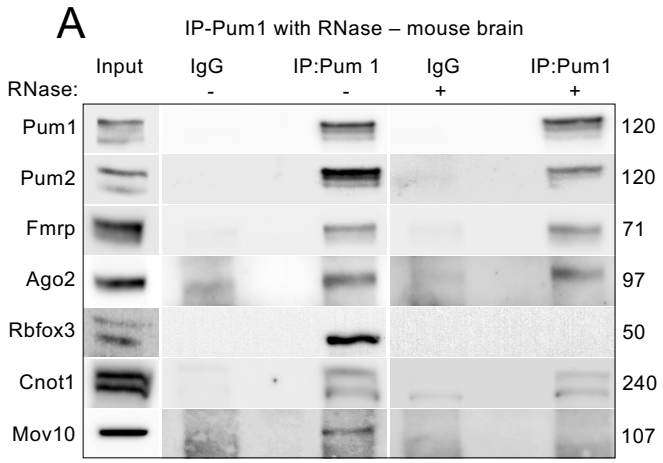

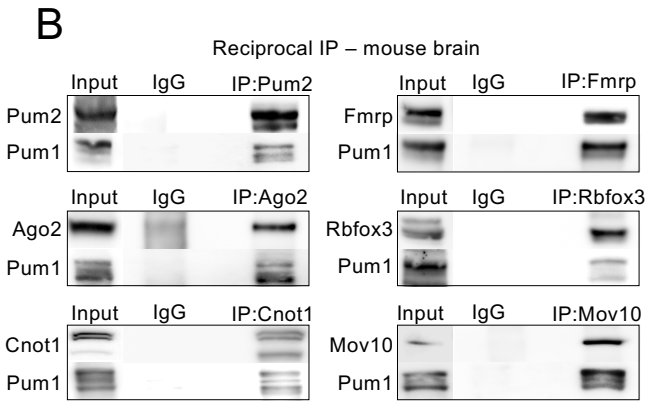

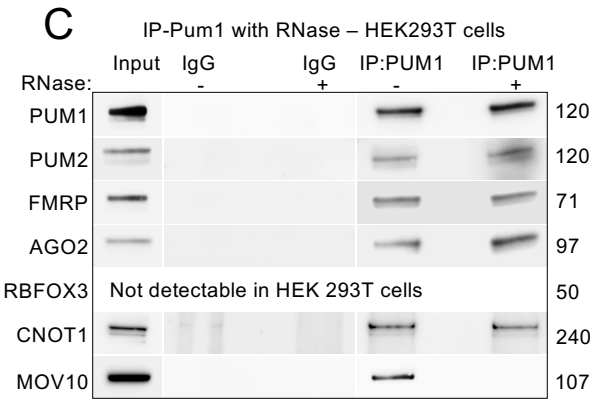

Figure 3, Botta et al.

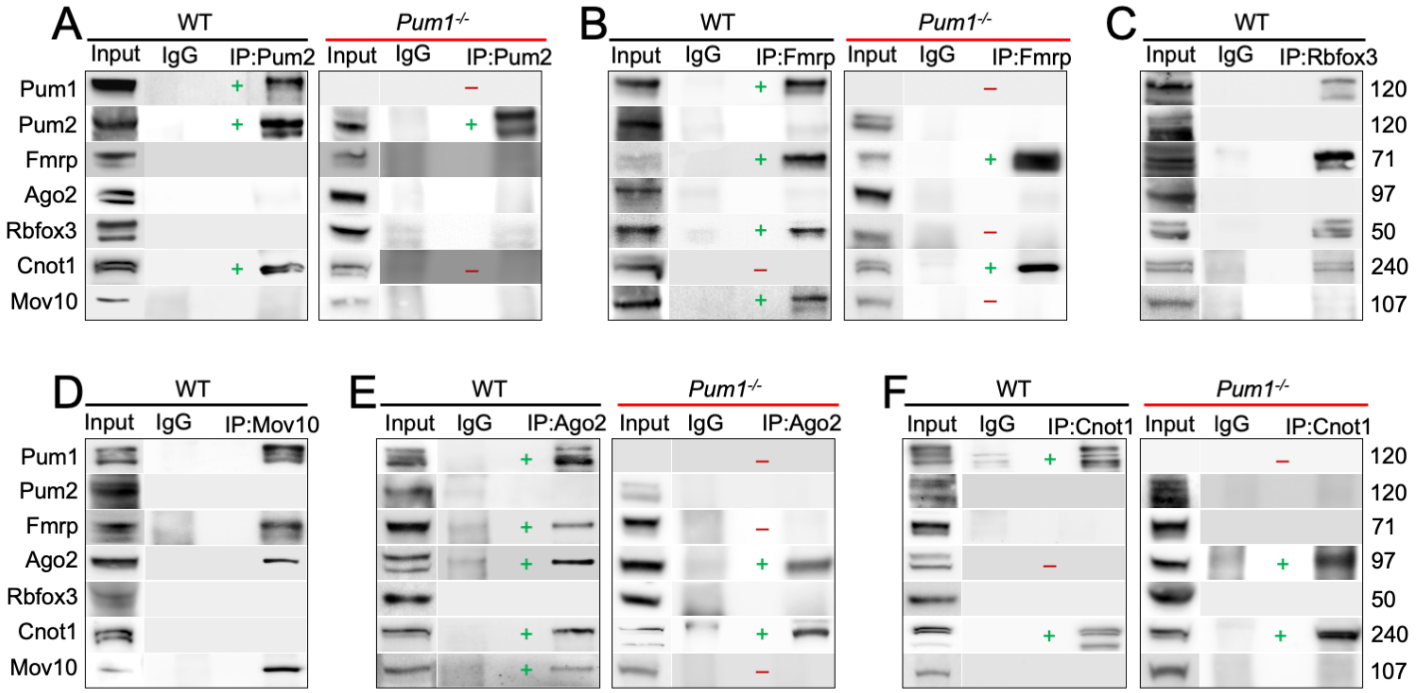

Figure 4, Botta et al.

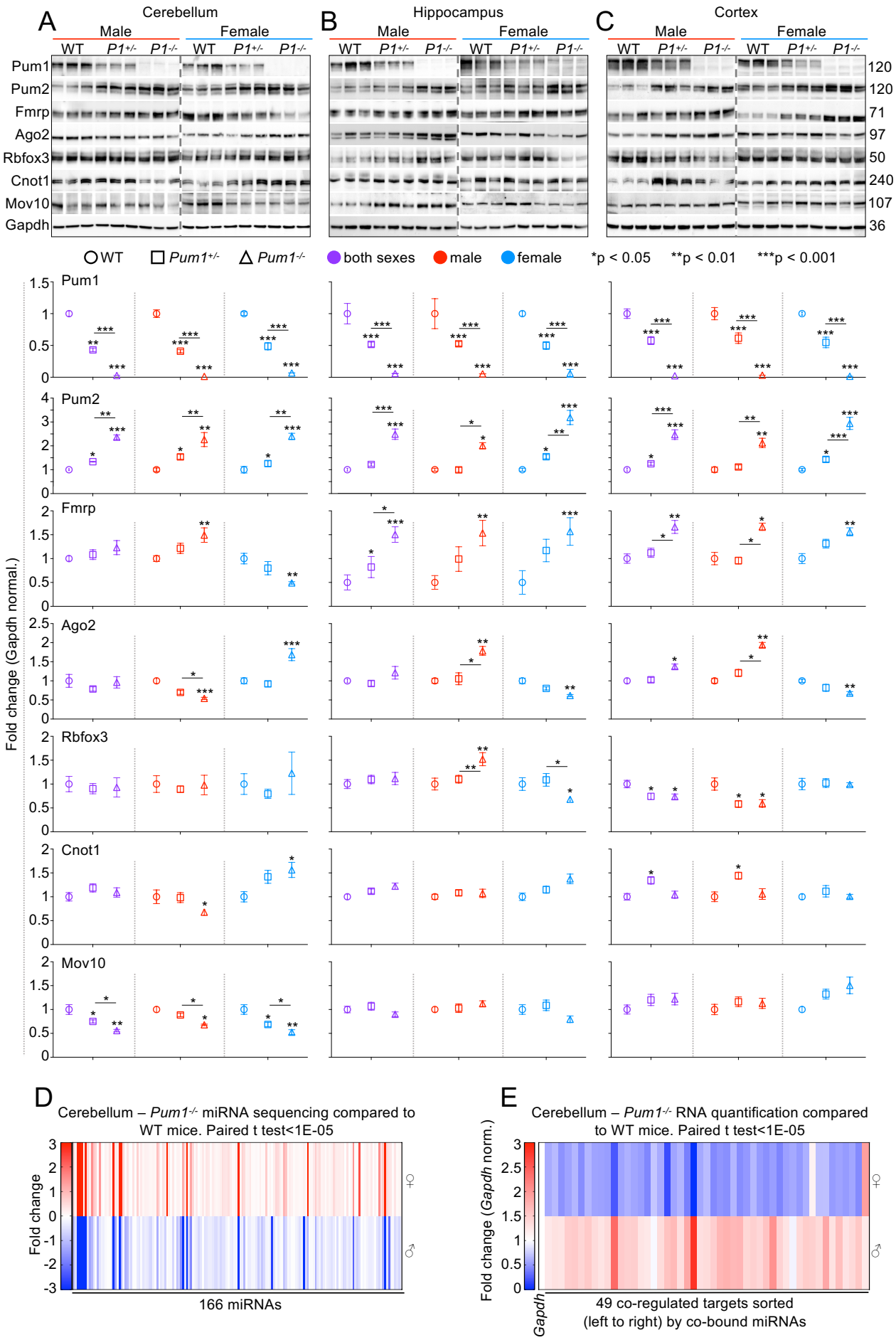

Figure 5, Botta et al.

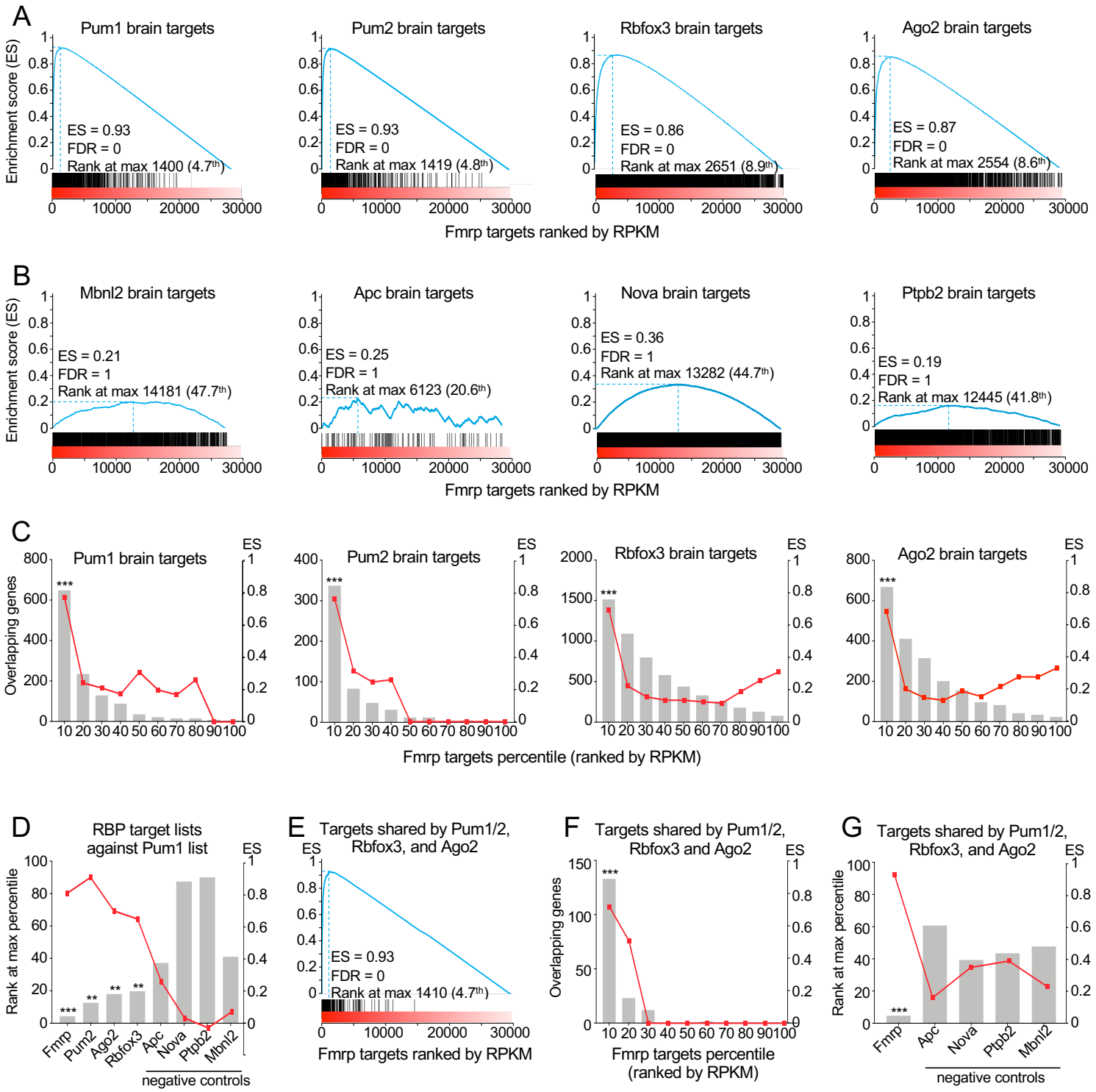

Figure 6, Botta et al.

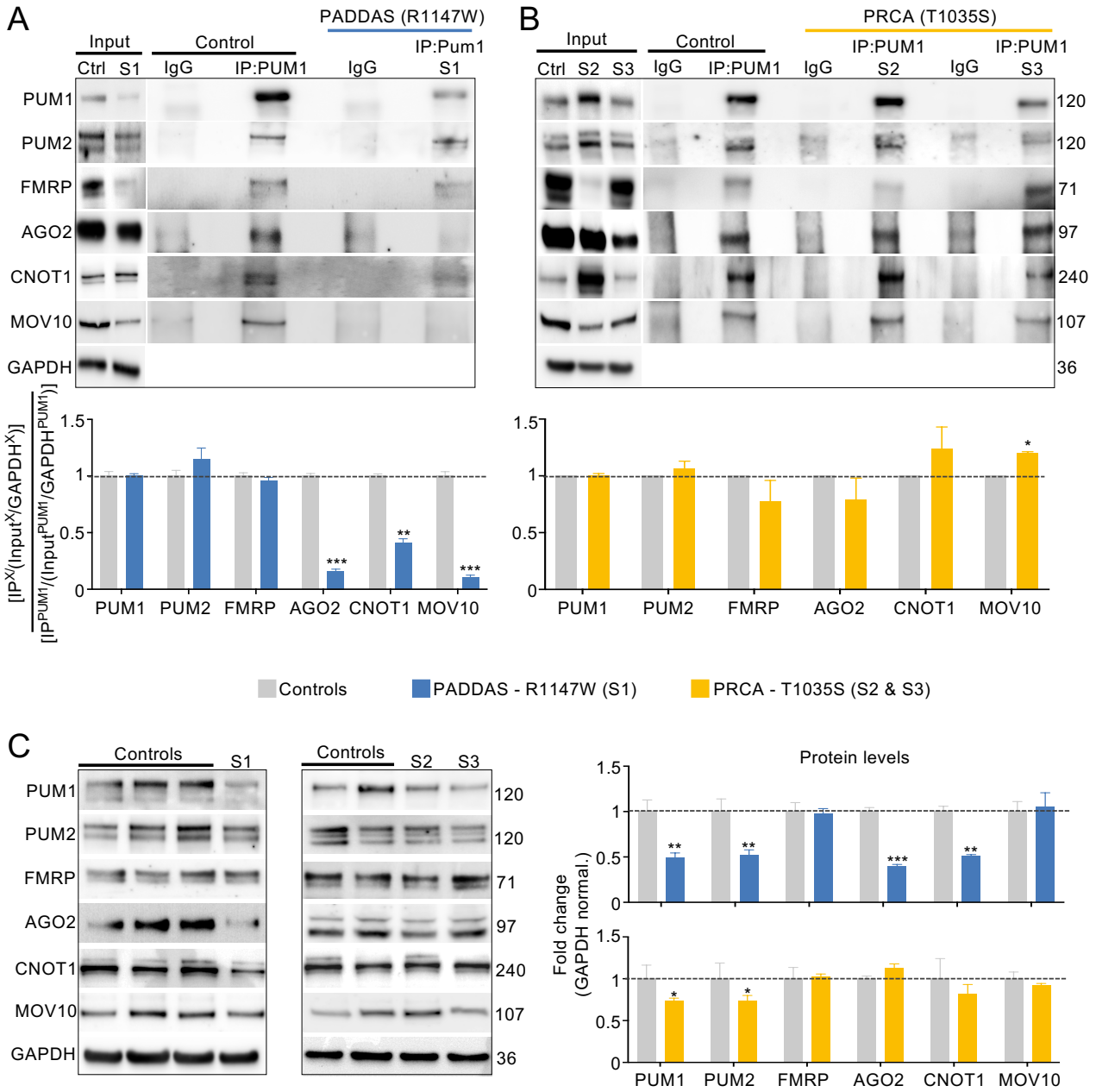

Figure 7, Botta et al.

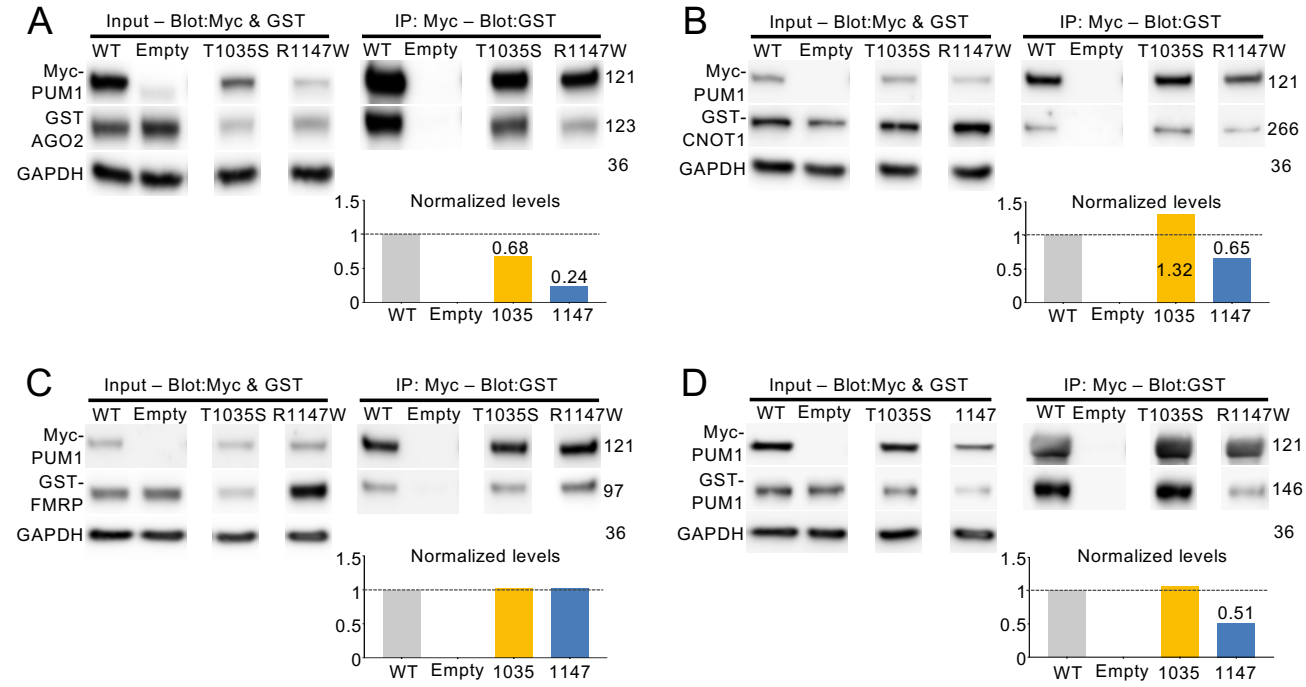

$$\text{IP Normalization} = \frac{[IP^{X}/(Input^{X}/GAPDH^{X})]}{[IP^{PUM1}/(Input^{PUM1}/GAPDH^{PUM1})]}$$

WT or Empty (E)

--- Age- and sex- matched control cell lines

R1147W PADDAS (S1)

T1035S PRCA (S2 & S3)

*p<0.05; **p<0.01; ***p<0.001

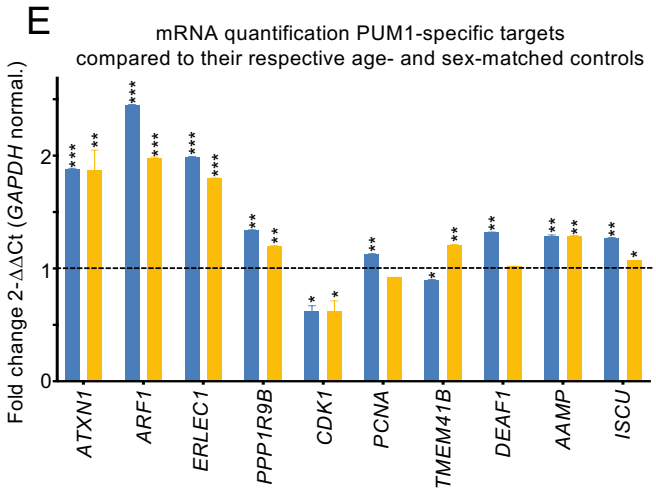

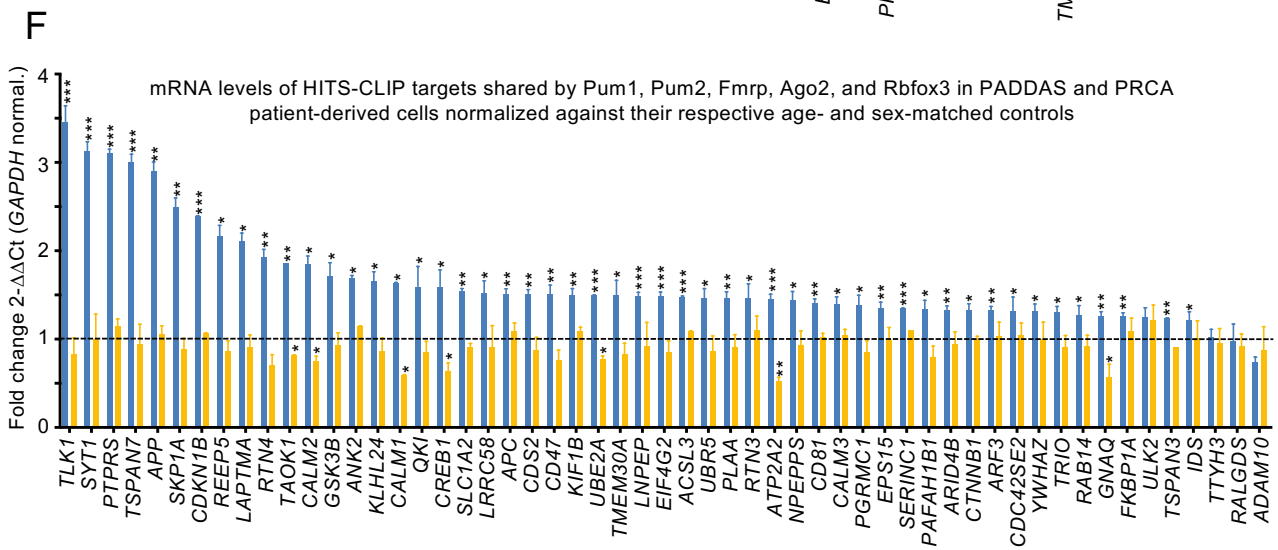

Figure S1, related to Figure 1, Botta et al.

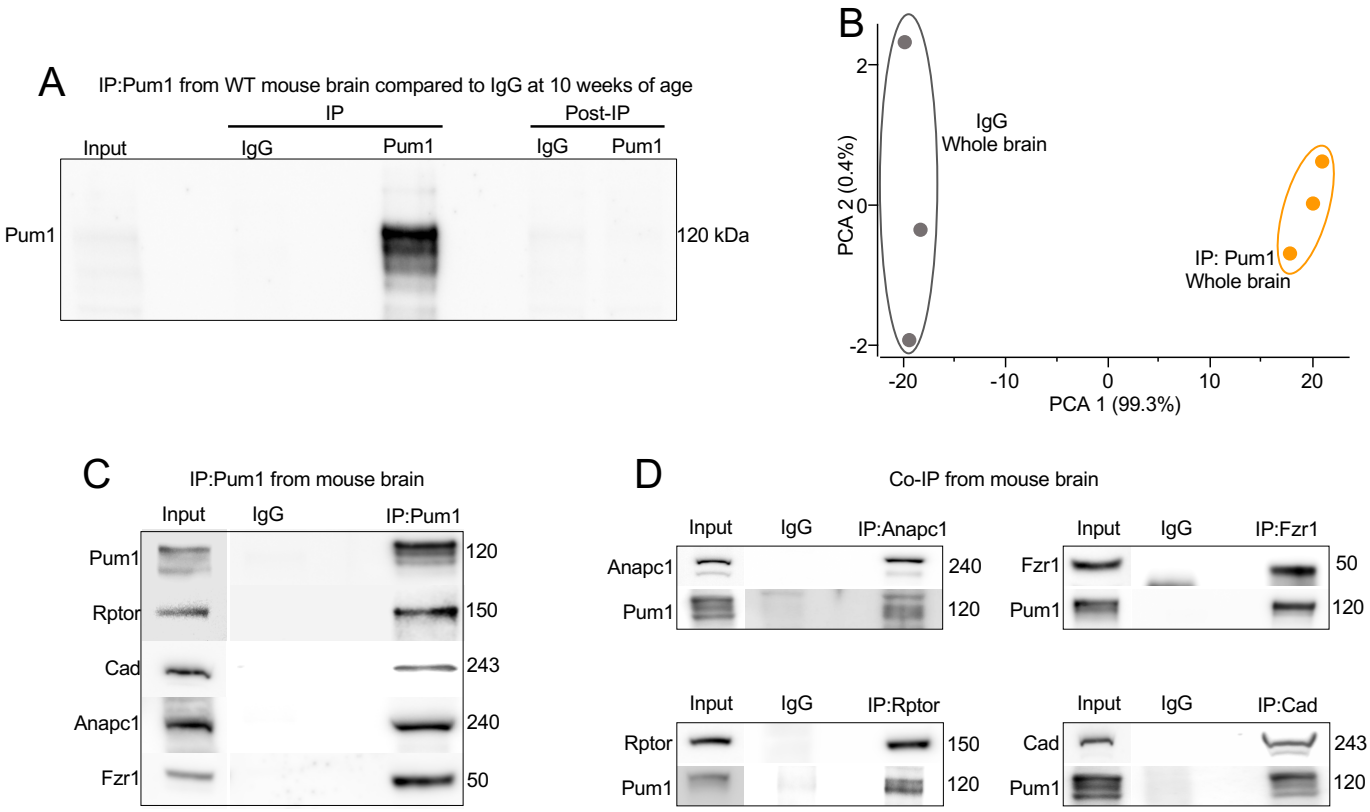

Figure S2, related to Figure 1, Botta et al.

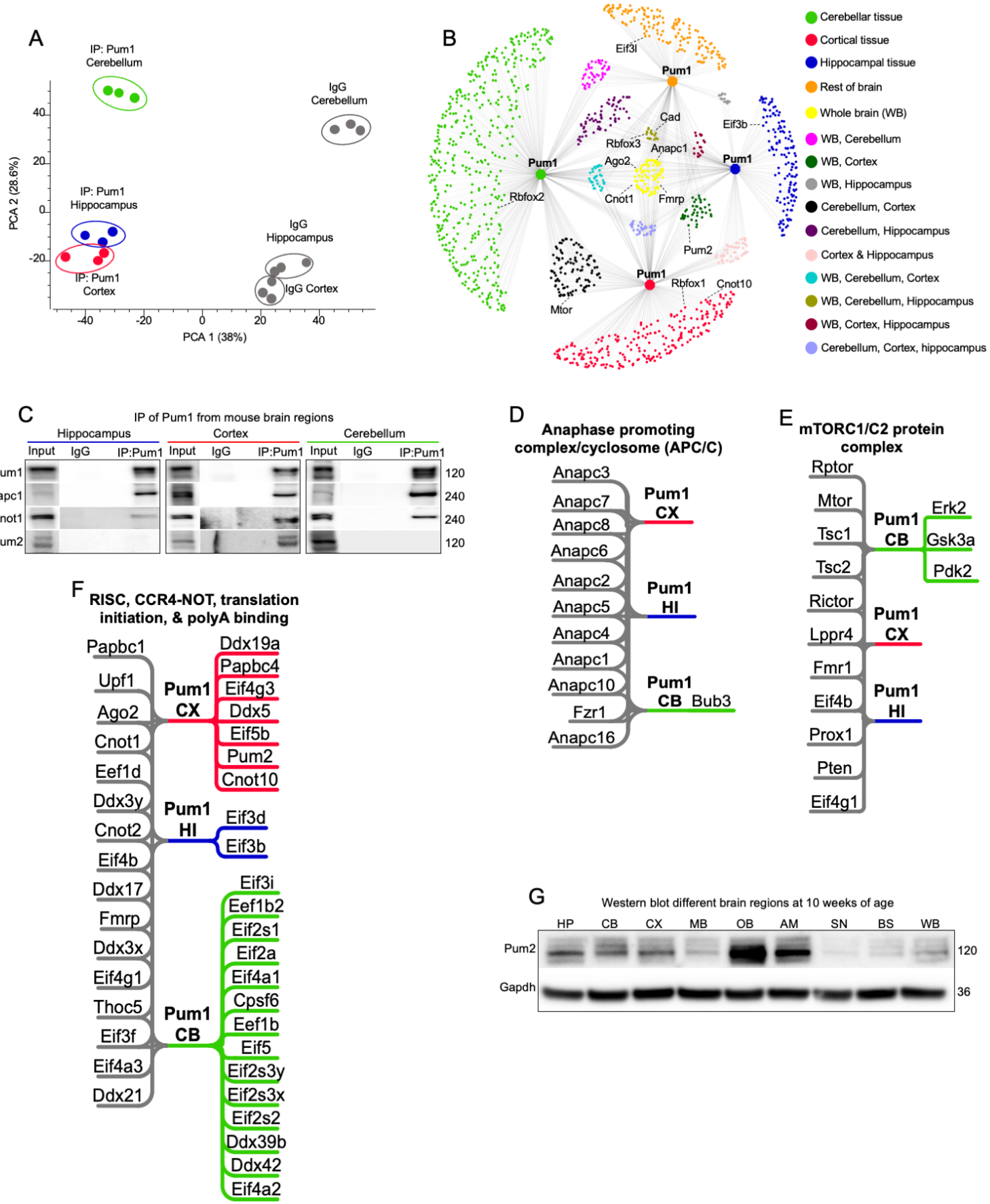

Figure S3, related to Figure 3, Botta et al.

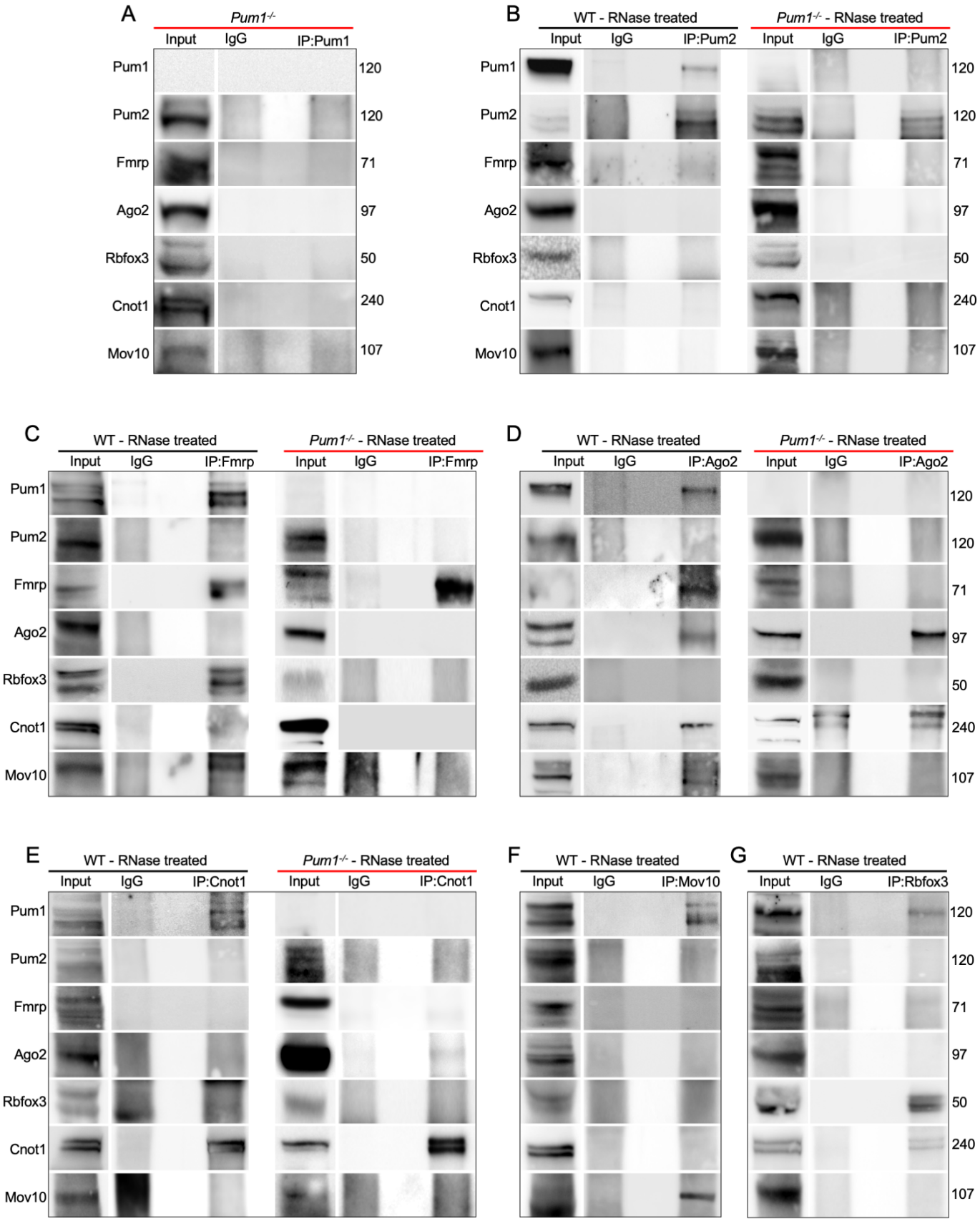

Figure S4, related to Figure 4, Botta et al.

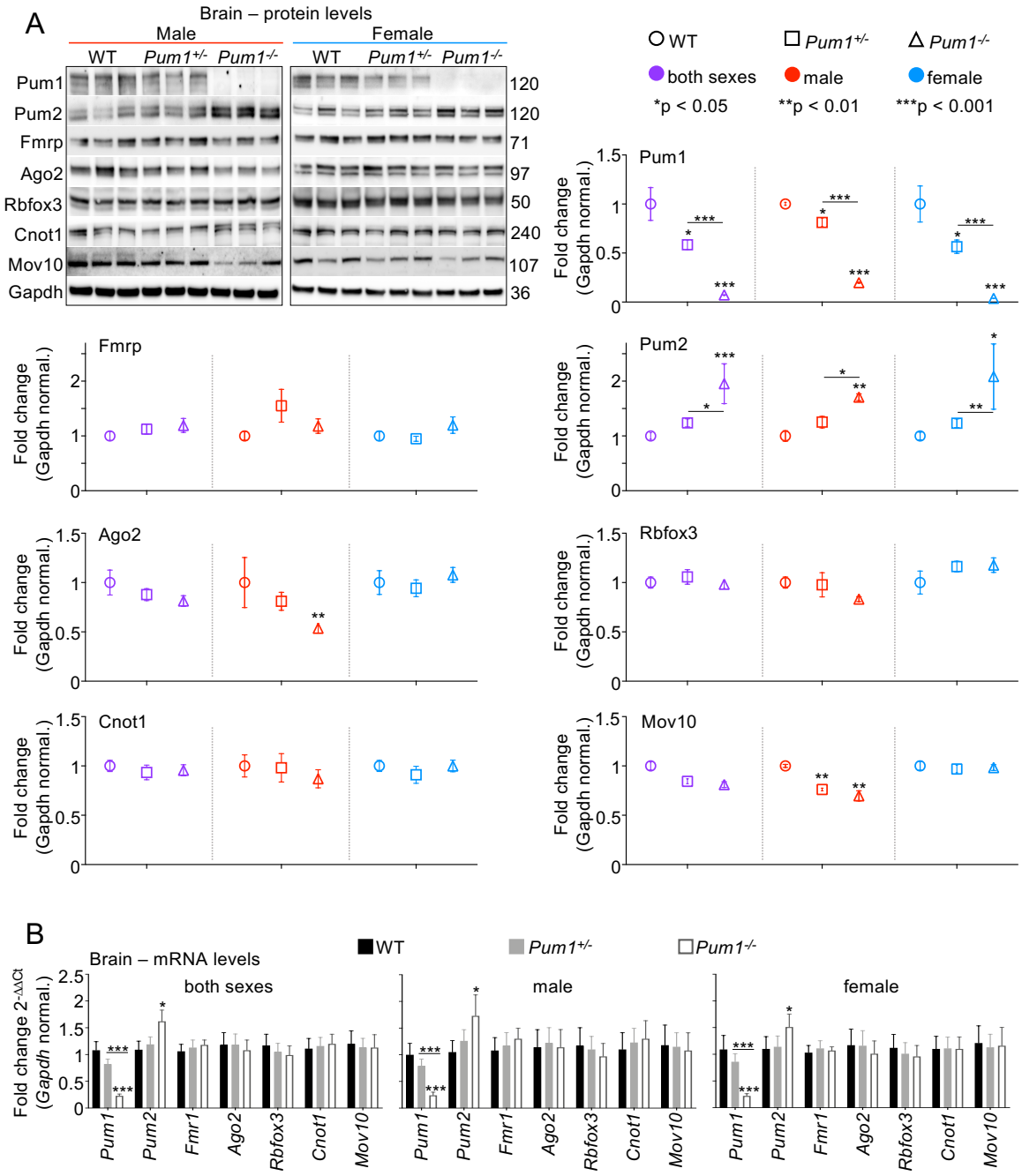

Figure S5, related to Figure 4, Botta et al.

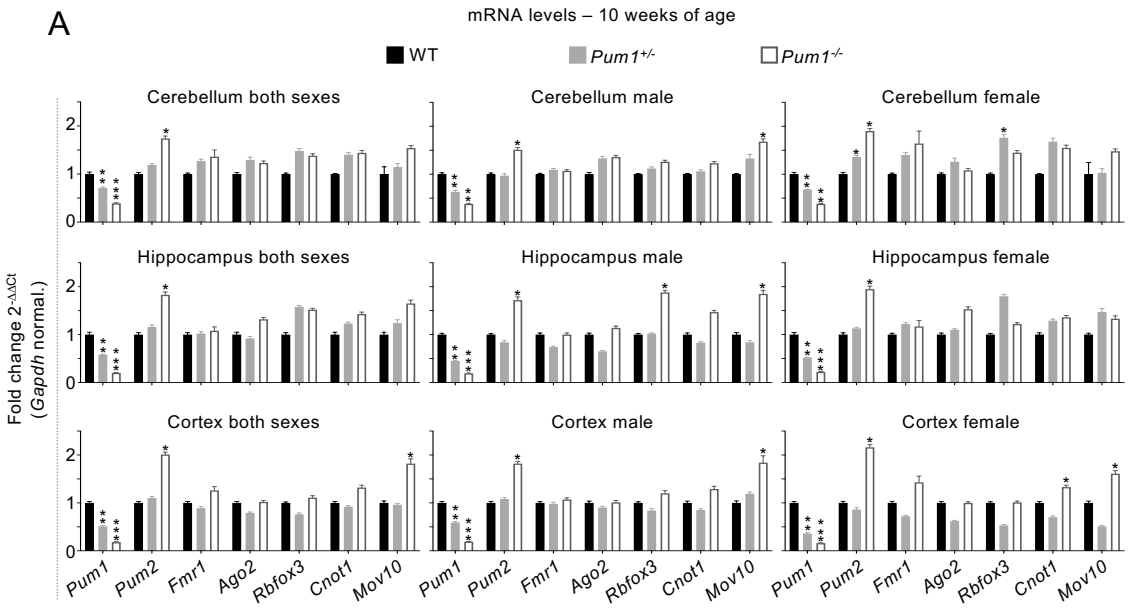

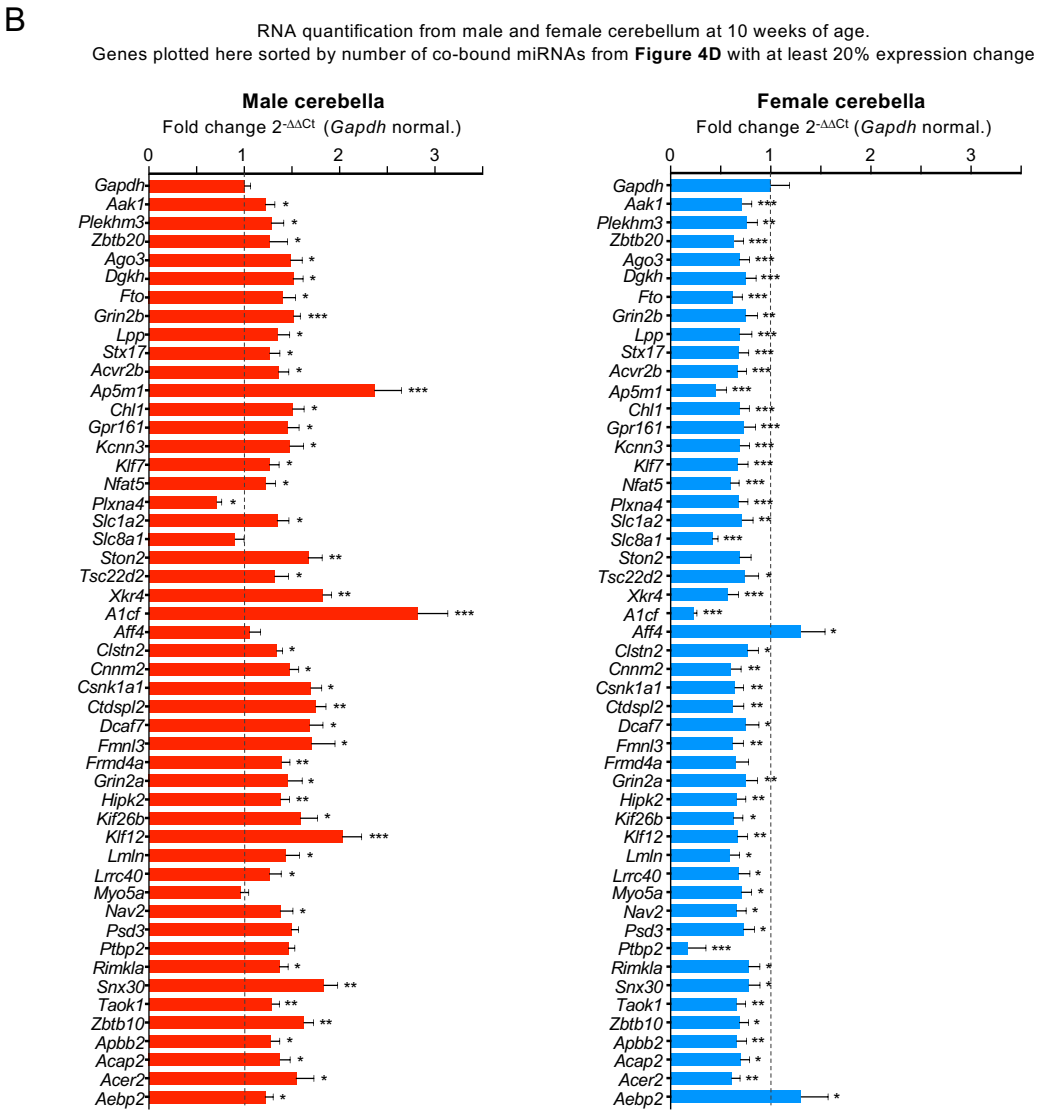

Figure S6, related to Figure 5, Botta et al.

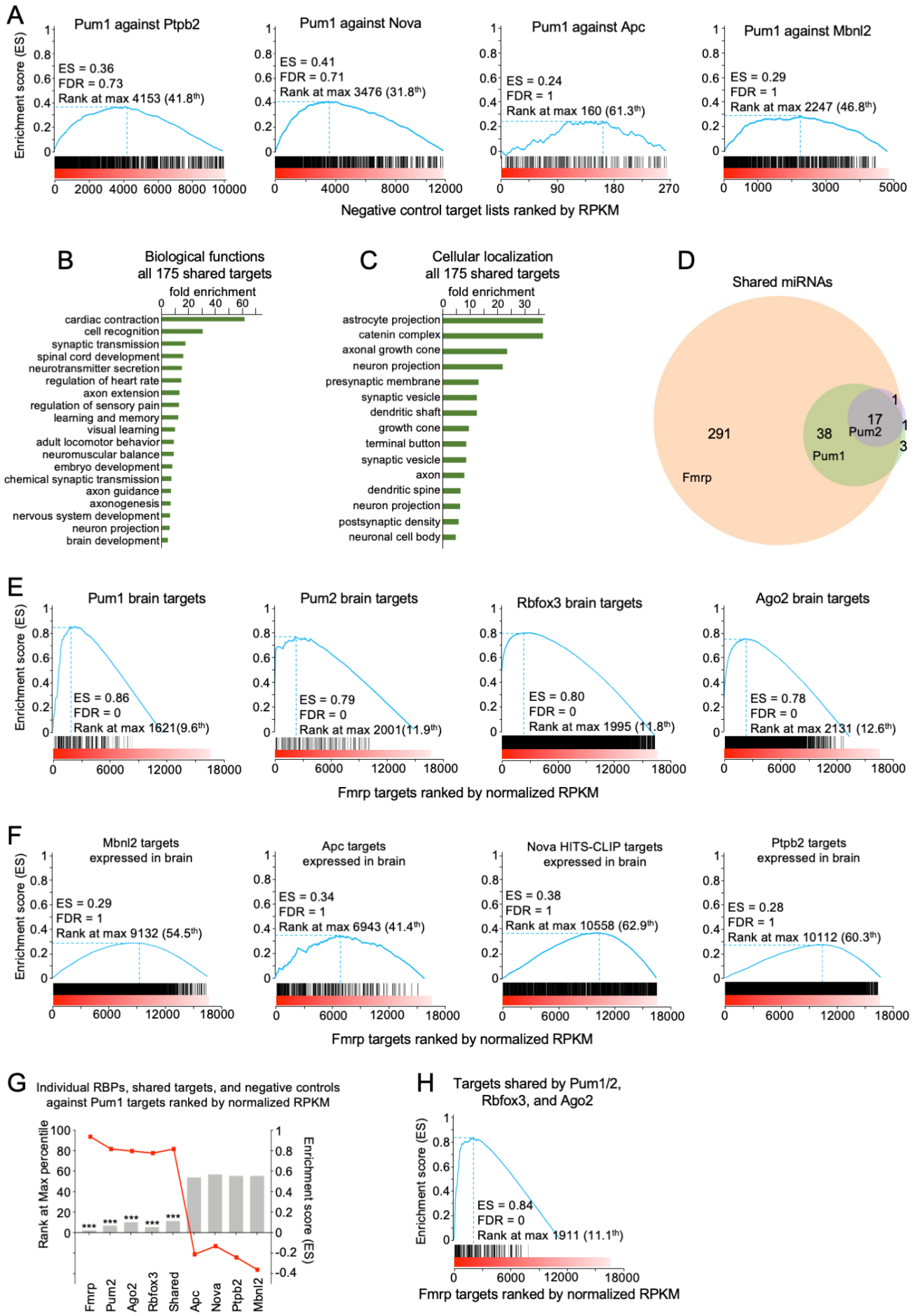
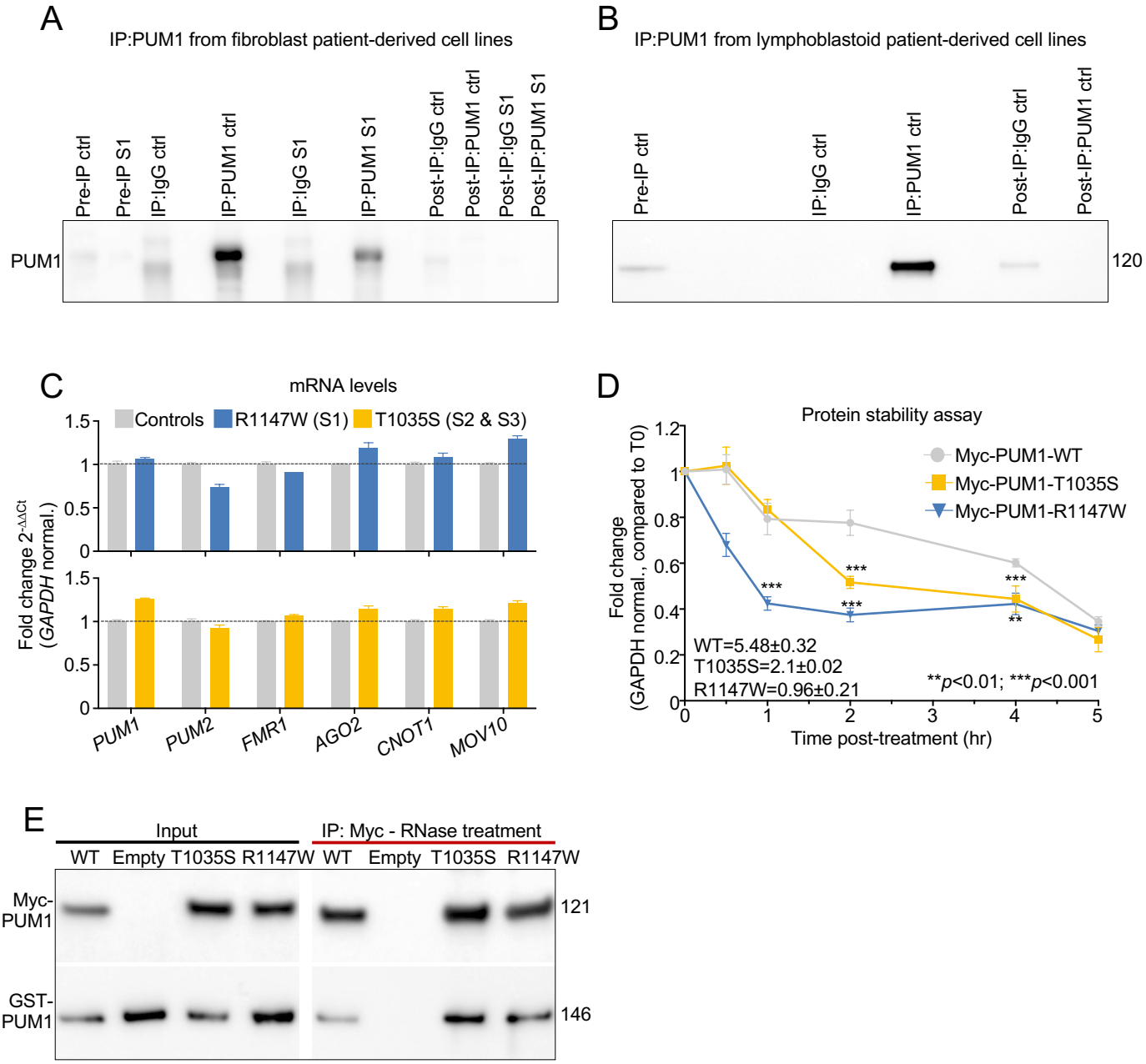
Figure S7, related to Figure 6, Botta et al.